

Multiplexed high-content analysis of mitochondrial morphofunction using live-cell microscopy

Elvio F Iannetti^{1,2}, Jan A M Smeitink^{2–4}, Julien Beyrath², Peter H G M Willems^{1,2,4} & Werner J H Koopman^{1,2,4}

¹Department of Biochemistry, Radboud Institute for Molecular Life Sciences, Nijmegen, the Netherlands. ²Khondrion BV, Nijmegen, the Netherlands.

³Department of Pediatrics, Radboud Center for Mitochondrial Medicine, Radboudumc, Nijmegen, the Netherlands. ⁴Centre for Systems Biology and Bioenergetics, Radboudumc, Nijmegen, the Netherlands. Correspondence should be addressed to W.J.H.K. (Werner.Koopman@radboudumc.nl).

Published online 18 August 2016; doi:10.1038/nprot.2016.094

Mitochondria have a central role in cellular (patho)physiology, and they display a highly variable morphology that is probably coupled to their functional state. Here we present a protocol that allows unbiased and automated quantification of mitochondrial ‘morphofunction’ (i.e., morphology and membrane potential), cellular parameters (size, confluence) and nuclear parameters (number, morphology) in intact living primary human skin fibroblasts (PHSFs). Cells are cultured in 96-well plates and stained with tetramethyl rhodamine methyl ester (TMRM), calcein-AM (acetoxy-methyl ester) and Hoechst 33258. Next, multispectral fluorescence images are acquired using automated microscopy and processed to extract 44 descriptors. Subsequently, the descriptor data are subjected to a quality control (QC) algorithm based upon principal component analysis (PCA) and interpreted using univariate, bivariate and multivariate analysis. The protocol requires a time investment of ~4 h distributed over 2 d. Although it is specifically developed for PHSFs, which are widely used in preclinical research, the protocol is portable to other cell types and can be scaled up for implementation in high-content screening.

INTRODUCTION

Mitochondria are cellular organelles that fulfill a wide range of functions in cellular metabolism¹. Within living cells, individual mitochondria are motile and display fission/fusion events^{2,3}. The balance between these processes, in combination with mitochondrial swelling/shrinking and removal of mitochondria by mitophagy, determines net mitochondrial morphology^{4,5}. Healthy mitochondria display an inside-negative electrical potential ($\Delta\psi$) across their inner membrane that is required to sustain mitochondrial ATP generation⁶ and can be considered as a semiquantitative functional readout of mitochondrial health^{7,8}. Functional defects in mitochondrial and/or cellular metabolism are often associated with aberrations in mitochondrial morphology and vice versa^{9–12}. Importantly, these defects are not only seen in rare monogenic mitochondrial disorders but are also associated with common pathologies such as Alzheimer’s disease, Parkinson’s disease, Huntington’s disease, cancer, cardiac disease, diabetes, epilepsy and obesity. Moreover, a progressive decline in the expression of mitochondrial genes is a central feature of normal human aging^{13,14}. This means that maintaining normal mitochondrial morphofunction is of eminent importance for human health and, as a consequence, strategies for evaluation of this morphofunction are a subject of major interest in experimental research, pharmacological screening and clinical diagnostics (reviewed in Tronstad *et al.*¹⁵). Mitochondrial structure and metabolism are tightly interfaced with the rest of the cell^{16,17}. Therefore, physiological analyses ideally are carried out using the natural mitochondrial ‘habitat’, being the cytosol of an intact living cell^{8,13,14,18}. In this respect, fluorescence microscopy is the most direct method for assessing live-cell mitochondrial morphofunction. During the past decade, we have established an integrated experimental and computational strategy for semiautomatic quantification of mitochondrial morphofunction, on which the current protocol is based. In brief, our previously published strategy consists of the following parts:

- Staining of mitochondria in living cells with reporter molecules such as mitochondria-targeted fluorescent proteins

(mtFPs)¹⁹ or fluorescent cations, including rhodamine 123 (refs. 20–22) and TMRM²³.

- Imaging of these cells^{22,24} using a climate-controlled (video-rate) confocal microscope^{20–22} or an epifluorescence microscope^{7,23,25}.
- Application of image processing techniques to allow extraction of relevant mitochondrial parameters such as fluorescence intensity and mitochondrial shape from the images (‘descriptors’).
- Statistical evaluation and/or mining of the descriptor data for phenotypic classification of different cell lines and drug effects^{26,27}.

Importantly, in developing the above approach, a ‘reverse strategy’ was followed, meaning that the descriptors that should be extracted from the microscopy images were first defined. Next, an image processing pipeline was designed to obtain these descriptor values. Then, the image properties that were required to allow successful descriptor extraction were determined. Finally, a cellular staining and image acquisition workflow compatible with these image requirements was implemented. Development of the protocol was initiated and first presented in 2005 for quantitative analysis of mitochondrial morphofunction in PHSFs^{20,21}. Using PHSFs from patients with mitochondrial disease, morphofunction was quantitatively compared with reactive oxygen species levels^{7,28}, cytosolic calcium homeostasis^{7,24}, enzyme activities²¹ and clinical data²⁶. In later years, the 2005 protocol was further validated using genetic mtFPs such as the enhanced yellow fluorescent protein^{19,29} and was successfully applied in other cell types (Supplementary Table 1 and the Supplementary References). In essence, our 2005 method involves manual acquisition of single microscopy images, followed by semiautomatic image processing and quantification. Here, this method is adapted for use with multiple reporter molecules (‘multiplexed’)³⁰ and 96-well plates. High-content (multidescriptor) analysis is particularly important in drug discovery, as therapeutic small molecules generally exert subtle pleiotropic effects via (a)specific targeting of (multiple) effectors, which might be overlooked by single-descriptor analysis^{27,31–33}. The protocol

PROTOCOL

presented here combines quantitative analysis of mitochondrial morphology and $\Delta\psi$ with that of cell size/confluence and nuclear number/morphology. After cell staining, each well is automatically imaged and analyzed (high throughput), yielding multiple descriptors (high content). We also provide an automated QC algorithm, which allows large-scale statistical evaluation and classification of mitochondrial morphofunctional phenotypes.

Comparison with other methods

Many strategies for the quantification of mitochondrial morphology have been presented in the literature, several of which are included in **Supplementary Table 1**. With respect to image quantification, these strategies are often similar to the one that we initially described for PHSFs^{20,21}. However, other studies were performed using different cell types (e.g., HEK293, HeLa and HUVECs) and fluorescent markers. In various studies, including our own, only a limited number of mitochondrial morphology descriptors were quantified³⁴. Fortunately, mitochondrial morphology can be described well using only a few ‘biologically relevant’ descriptors (i.e., the number of mitochondria per cell, mitochondrial size, mitochondrial mass, mitochondrial aspect ratio and mitochondrial formfactor¹⁵). However, using a relatively low number of descriptors might be disadvantageous for phenotypic analysis and/or drug-screening studies²⁷. As an alternative to our presented PCA-based strategy, mitochondrial morphology can also be analyzed by machine-learning strategies³⁵. For instance, unsupervised machine learning was applied to define six morphological phenotypes in CHO cells and the effects thereupon of caspase inhibition³⁶. Similarly, supervised machine-learning and fuzzy logic methods were used to study mitochondrial morphology, $\Delta\psi$ and Bax activation in human epithelial cells treated with mitochondrial inhibitors^{37,38}. In these two studies, classification of mitochondrial shape was based on three predefined phenotypes ('tubular', 'donut-shaped' and 'swollen'). A similar approach was applied in another machine-learning study³⁹. In contrast to the protocol presented here, these predefinition strategies might introduce an undesirable bias. Therefore, we recently used a supervised machine-learning approach for data mining and visualization, but, similar to the current protocol, we did not assume the existence of predefined mitochondrial morphology phenotypes²⁷.

Limitations of the protocol

A limitation of this method is that the cell seeding and staining procedures have to be carried out manually, which requires time investment. Moreover, because a nonconfocal mode of imaging is used, the protocol performs best with relatively large cells displaying a flat morphology (e.g., PHSFs). This is because results obtained by 2D image analysis are representative of 3D mitochondrial morphofunctional properties in such cells⁴⁰. When analysis of 'thick' and/or small cells is required, the protocol can be adapted using the information provided in the Troubleshooting section; otherwise, alternative strategies should be used. The latter include 3D mitochondrial morphology analysis, super-resolution microscopy and 2-photon microscopy^{41–46}. In contrast to those from other studies³⁹, the numerical data obtained in this protocol represent average descriptor values for each image/well (i.e., containing multiple cells). This means that data for individual cells are not available. In its current form,

the presented protocol cannot be used to quantify mitochondrial motility or ultrastructure. However, in this respect, various other strategies have been described^{47–53}.

Experimental design

Overview of the protocol. The full protocol is summarized in a flowchart (**Fig. 1**), and it combines three fluorescent reporter molecules into a single live-cell assay. PHSFs are cultured on 96-well plates, after which the main emphasis is on the correct use of the mitochondria-selective fluorescent cation TMRM to quantify mitochondrial morphology and $\Delta\psi$. To this end, cells are also stained with calcein and Hoechst 33258 (Hoechst) to coassess cellular and nuclear parameters, respectively. For each well, a TMRM, calcein and Hoechst image is acquired (**Fig. 1a**) and processed (**Fig. 1b,c**) to extract quantitative descriptors (**Table 1**). From the TMRM images, 33 different descriptors are extracted, including the mitochondrial aspect ratio (AR; a measure of mitochondrial length), the average mitochondrial TMRM signal (Dm; a semi-quantitative measure of $\Delta\psi$) and the mitochondrial 'roundness' (or formfactor (F), a combined measure of mitochondrial length and degree of branching). The calcein image is used to quantify the total cell area (CaSum) and integrated intensity (CaIOD). Hoechst staining is analyzed to determine the total number of nuclei (Nn), as well as their area (An) and formfactor (Fn). Integration of the various descriptors allows calculation of various 'derived descriptors', including the cell-size-corrected mitochondrial mass (Mm), mitochondrial size (Am; Am = Asum/Ot), the number of mitochondria per cell (Nc) and cell size (Casum/Nn). In total, automated image processing and quantification (**Fig. 1b**) yields a total of 44 descriptors for each well for further analysis (**Fig. 1c**).

Fluorescent reporters. TMRM (**Fig. 2a**) is a fluorescent lipophilic cation that accumulates within the mitochondrial matrix in a $\Delta\psi$ -dependent manner. This results in a mitochondria-specific fluorescence signal that allows the analysis of mitochondrial morphology and semiquantitative $\Delta\psi$ analysis. TMRM is maximally excited by 552-nm light and maximally emits fluorescence light at 578 nm (**Fig. 2b**). Importantly, matrix accumulation of TMRM depends not only on $\Delta\psi$, but also on the electrical potential of the plasma membrane (ΔV ; ref. 7). Therefore, if there is doubt about potential ΔV changes, they should be quantified using electrophysiological techniques⁵⁴ or an alternative strategy⁵⁵. In addition, when its concentration in the mitochondrial matrix exceeds a certain threshold, TMRM quenches its own fluorescence ('autoquenching'). This leads to a reduction in the TMRM fluorescence signal and erroneous underestimation of $\Delta\psi$. When illuminated using an inappropriately high excitation intensity or for a long period of time, TMRM can display substantial photobleaching and, by acting as a photosensitizer, can stimulate the opening of the mitochondrial permeability transition pore^{56–58}. Of note, to detect hyperpolarization (i.e., $\Delta\psi$ values becoming more negative) TMRM needs to be present outside the cells during the measurement⁵⁴. Calcein is used to label living cells in cell viability and cytotoxicity assays⁵⁹. Its nonfluorescent AM form (calcein-AM) is taken up by the cells. There it is converted by intracellular esterases into the fluorescent and hydrophilic calcein molecule by cleavage of its AM tail (**Fig. 2a**). This process traps the calcein inside the cell. Calcein is maximally excited by 493-nm light, and it maximally emits fluorescence light at 514 nm (**Fig. 2b**).

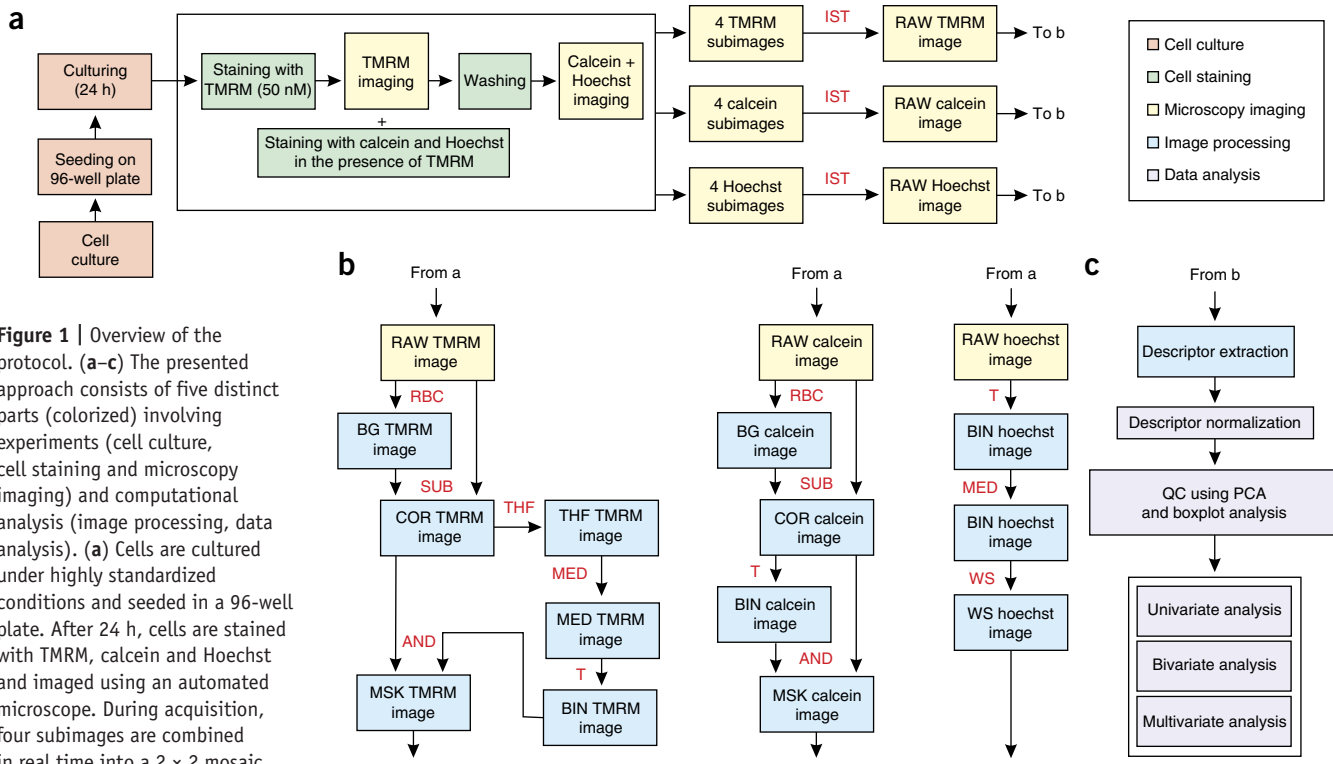


Figure 1 | Overview of the protocol. (a–c) The presented approach consists of five distinct parts (colorized) involving experiments (cell culture, cell staining and microscopy imaging) and computational analysis (image processing, data analysis). (a) Cells are cultured under highly standardized conditions and seeded in a 96-well plate. After 24 h, cells are stained with TMRM, calcein and Hoechst and imaged using an automated microscope. During acquisition, four subimages are combined in real time into a 2×2 mosaic using image stitching (IST).

This yields 3 ‘RAW’ images (TMRM, calcein and Hoechst) for each well. (b) Image processing pipeline for the RAW images obtained in a. After processing, each RAW image is converted into an image suited for descriptor extraction: a ‘masked’ TMRM image (MSK TMRM), a ‘masked’ calcein image (MSK calcein) and a ‘watershed’ Hoechst image (WS Hoechst). (c) Descriptor data are extracted from the processed images, normalized and subjected to a QC step. The resulting data set can then be analyzed and visualized by various means (see main text for details). AND, Boolean AND operator; BG, background image; BIN, binary image; COR, background-corrected image; MED, median-filtered image; MSK, masked image; RAW, image directly from microscope; RBC, rolling-ball correction; SUB, background subtraction; T, thresholding; THF, top-hat filter; WS, watershed operation.

Of note, AM-ester-based fluorescent molecules, but not their de-esterified forms, can be actively extruded from the cell by multidrug transporters⁶⁰. Hoechst (Fig. 2a) is one of the most widely used stains for DNA quantification. It is a cell-permeable fluorescent molecule that specifically binds to the A-T base pairs in the minor groove of double-stranded DNA (dsDNA). By itself Hoechst displays a weak fluorescence, which is greatly enhanced upon DNA binding. Hoechst is maximally excited by 352-nm light and maximally emits fluorescence light at 455 nm (Fig. 2b).

Microscopy hardware. In this protocol, a BD Pathway 855 system (Fig. 2c–e) is used to perform automated image acquisition. This microscope is equipped with an environmental control system (temperature and CO₂), which is necessary for live-cell imaging, and a shielded measuring chamber that prevents interference from ambient light. It also features an automated pipetting robot, which is not used in this protocol. Excitation light is provided by two mercury arc lamps (Lamp A and Lamp B; Figs. 2d and 3a,b), from which the required wavelength is selected by two excitation filter wheels (Wheel A and Wheel B). Excitation light intensity can be independently controlled for both lamps via two dichroic mirror wheels (Wheel 1 and Wheel 2); excitation light is directed to the cells via an air (dry) 40 \times objective. In this protocol, wide-field images are acquired, and therefore the spinning disk confocal optics of the Pathway 855 system are not

used. TMRM/calcein/Hoechst emission light is directed toward a cooled CCD (charge-coupled device) camera via Wheel 2 and an emission filter wheel. Taking into account the spectral properties of the reporter molecules (Fig. 2b), appropriate excitation ('Ex'), dichroic ('Dich') and emission ('Em') filters were selected (Fig. 3c–e). This allowed acquisition of specific TMRM, calcein and Hoechst fluorescence images from co-stained cells.

Image acquisition and image properties. The cell lines to be analyzed are seeded in a column-wise manner on the 96-well plate (see the ‘Control cell lines and replicates’ section for details) and imaged using the ‘ZIG-ZAG’ scanning mode option (Fig. 4). Automatic focusing is carried out using an integrated laser-based autofocus system. The microscope stage was motionless, so images of subsequent wells were acquired by moving the objective. For each well and reporter molecule, four subimages with a bit depth of 12-bit (i.e., containing a maximum of 4,096 grayvalues) were acquired and automatically combined during acquisition by ‘image stitching’ (Fig. 1a). The resulting 2×2 RAW image was stored as an uncompressed 16-bit TIFF (tagged image file format) file (i.e., with a range of $2^{16} = 65,536$ grayvalues) having a file size of 2,679 kb. Each RAW image had a dimension of 1,344 \times 1,024 pixels (equalling 210.5 $\mu\text{m} \times$ 160.4 μm). In total, 288 RAW images were obtained for each plate (with a total file-size of 771 Mb) and stored to the hard-disk.

PROTOCOL

TABLE 1 | Descriptors calculated for each well.

No ^a	Reporter	Descriptor	Symbol	Definition/meaning of descriptor ^b
1	TMRM	Aspect ratio	AR	Ratio between major axis and minor axis of an ellipse equivalent to the object: measure of mitochondrial length
2	TMRM	Area/Box	Ab	The ratio between the area of an object and the area of its bounding box
3	TMRM	Box XonY	Bxy	Ratio between the width and height of the object's bounding box
4	TMRM	Density mean	Dm	Average intensity of the object (grayvalue): average mitochondrial intensity of the TMRM signal
5	TMRM	Axis minor	Axm	Length of the minor axis of the ellipse with same moments of order 1 and 2 as the object (pixels)
6	TMRM	Diameter max	Dimax	Length of the longest line joining two points of the object's outline and passing through the object's centroid (pixels)
7	TMRM	Diameter min	Dimin	Length of shortest line joining two points of the object's outline and passing through the object's centroid (pixels)
8	TMRM	Diameter mean	Dim	Average length of diameters measured at 2-degree intervals and passing through the object's centroid
9	TMRM	Radius max	Rmax	Maximum distance between the object's centroid and outline (pixels)
10	TMRM	Radius min	Rmin	Minimum distance between the object's centroid and outline (pixels)
11	TMRM	Perimeter ellipse	Pe	The perimeter of the ellipse surrounding the outline of each object (pixels)
12	TMRM	Radius ratio	Rr	Ratio between Rmax and Rmin
13	TMRM	Roundness	F	Perimeter ² /(4 × π × Area; AKA formfactor): measure of mitochondrial length and degree of branching
14	TMRM	Length	Le	Feret diameter (caliper length) along the major axis of the object (pixels)
15	TMRM	Width	Wi	Feret diameter (caliper length) along the minor axis of the object (pixels)
16	TMRM	Perimeter2	P2	Chain code length of the outline (pixels)
17	TMRM	IOD	IOD	Integrated optical density of all objects (grayvalue): sum of all mitochondrial TMRM pixel intensity values
18	TMRM	Perimeter convex	Pc	Perimeter of the convex outline of the object (pixels)
19	TMRM	Perimeter	Pe	Length of the object's outline (pixels)
20	TMRM	Perimeter ratio	Pr	Ratio of convex perimeter to perimeter
21	TMRM	Area polygon	Ap	Area included in the polygon defining the object's outline (same polygon as used for Perimeter)
22	TMRM	Count	Cou	Size-weighted object 'count' (number of objects)
23	TMRM	Box width	Bw	Width of the object's bounding box (pixels)
24	TMRM	Box height	Bh	Height of the object's bounding box (pixels)
25	TMRM	Feret min	Fmin	Smallest feret (caliper) length (pixels)
26	TMRM	Feret max	Fmax	Longest feret (caliper) length (pixels)
27	TMRM	Feret mean	Fm	Average feret (caliper) length (pixels)
28	TMRM	Density min	Dmin	Minimum density inside the object (grayvalue)

(continued)

TABLE 1 | Descriptors calculated for each well (continued).

No ^a	Reporter	Descriptor	Symbol	Definition/meaning of descriptor ^b
29	TMRM	Density max	Dmax	Maximum density inside the object (grayvalue)
30	TMRM	Density s.d.	Dstdv	Standard deviation of intensity or density inside the object (grayvalue)
31	TMRM	Margination	Ma	The distribution of intensity between the center of an object and the edge of the object
32	TMRM	Area sum	Asum	Total area of the mitochondrial objects (pixels). The average size of the mitochondrial objects (A_m) is given by $Asum/Ot$
33	TMRM	Objects total	Ot	Total number of objects: total number of mitochondria
34	Calcein	Area sum	Casum	Total area of the objects (pixels)
35	Calcein	IOD sum	CaIOD	Integrated pixel intensity of the objects (grayvalue)
36	Hoechst	Nn	Nn	Total number of objects: total number of nuclei/cells (assuming 1 nuclear object per cell)
37	Hoechst	H. area	An	Average area of the objects (pixels): average area of the nuclei
38	Hoechst	H. roundness	Fn	Roundness of objects: describing nuclear shape
39	Derived	Cell mito ratio	Mm	Given by Asum/Casum: A measure of mitochondrial mass
40	Derived	Norm mito area	Amt	Given by Asum/Nn: equaling the total mitochondrial area (in pixels) per cell
41	Derived	Norm mito number	Nc	Given by Ot/Nn : equaling the average number of mitochondrial objects per cell. $Asum/Ot$ equals the area (size) of individual mitochondrial objects (A_m)
42	Derived	Norm cyto area	Casum/Nn	Average size of the object (pixels): a measure of average cell size
43	Derived	Confluence (%)	C%	Fraction/percentage of the image covered: a measure of cell confluence
44	Derived	Calcein fluorescence	CaIOD/ Casum	Average intensity per cellular pixel

^aCorresponding to the number of the descriptor in the provided MATLAB m-file (*Iannetti_MATLAB.m*). ^bAdapted from the definitions in the Image Pro Plus software. Where the unit measurement is not differently specified in parentheses after the meaning in the definition column, it is arbitrary units (a.u.). The first 31 descriptors were used in a previous study for PCA and machine learning²⁷.

Image processing and descriptor extraction. Automated image processing and descriptor extraction/calculations are carried out using Image Pro Plus (IPP) and MATLAB software. Once acquired, each RAW TMRM, calcein and Hoechst image (set) is processed independently (**Fig. 1b**). The processing pipeline for each reporter molecule is described in more detail directly below.

From the RAW TMRM image (**Fig. 5a**; left panel of top row), a background image was calculated using the ‘rolling ball’ correction algorithm^{61,62}. This algorithm filters out objects and requires one parameter: the rolling ball ‘feature width’. The latter should be set to at least the size of the largest object that is not part of the background. For TMRM-stained PHSFs, a feature width of 140 was empirically determined. Subtraction of the background image from the RAW image yielded a background-corrected image (COR). The COR image was processed using a top-hat spatial filter (THF, 7 × 7 kernel, 1 pass, strength 10). The top-hat filter functions as a ‘particle isolator’ that increases the grayvalue of mitochondrial objects (see **Box 1** for details). To remove noise pixels, the THF image is subsequently median-filtered (MED, 3 × 3 kernel, 6 passes; see **Box 1**) and ‘thresholded’ to yield a binary (BIN) image. An optimal threshold (T) value of 40 grayvalues was empirically determined

(**Supplementary Fig. 1** and the **Supplementary References**). In the BIN image, white mitochondrial objects (grayvalue of 65,535) are represented on a black background (which has a grayvalue of 0). Finally, the COR image is combined with the BIN image using a Boolean AND operator. This operator will keep only pixels that are ‘on’ (i.e., that have a grayvalue that is not 0) in both the COR and BIN images. This generates a ‘masked’ image (MSK) in which the background is black (grayvalue = 0) and each mitochondrial object pixel retains its TMRM grayvalue from the COR image. The MSK image (**Fig. 5a**; left panel of lower row) is used for descriptor extraction. The various processing steps of the TMRM images (**Fig. 1b**) are summarized in **Figure 5b**. Once the MSK image is obtained, a look-up table (LUT) can be used to color-code intensity values (**Fig. 5b**; ‘MSK+LUT’ image). As a first example of data visualization, mitochondrial objects can be sorted to yield a ‘mitogram’ according to the numerical value of a specific descriptor, here according to their formfactor (F ; **Fig. 5c**; left panel). Magnification of the mitogram (white box) can be used to visually inspect heterogeneities in TMRM staining for individual mitochondrial objects (F ; **Fig. 5c**; right panel). Quantification of mitochondrial descriptors in the mitogram (**Fig. 5d**) can, for

PROTOCOL

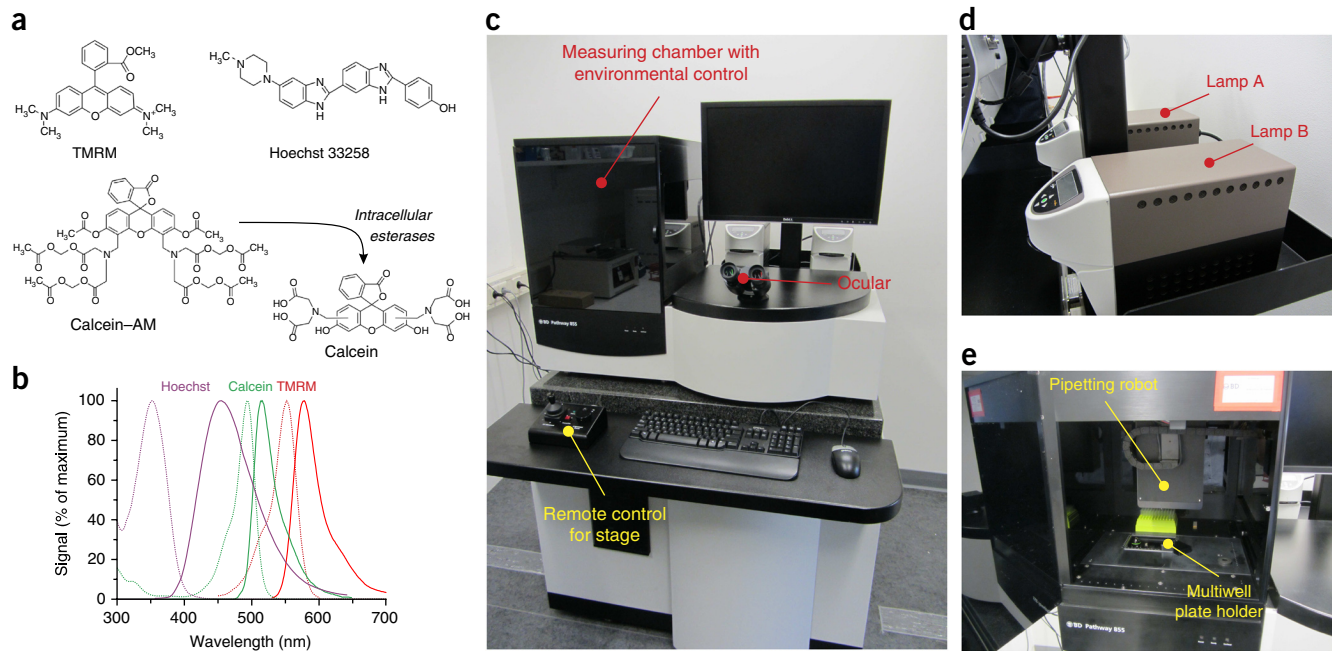


Figure 2 | Spectral properties of the fluorescent reporter molecules and microscopy hardware. (a) Chemical structures of TMRM, calcein-AM, calcein and Hoechst 33258 ('Hoechst'). Structures were obtained from <http://www.lifetechnologies.com>. (b) Excitation (dotted lines) and emission (continuous lines) of the used reporter molecules. Spectral information was obtained from <http://www.chroma.com>. (c) Front-view of the BD Pathway 855 automated microscopy system showing the light-shielded and environment-controlled measuring chamber, the ocular and the remote control of the microscopy stage. (d) View of the two mercury arc lamps (lamp A and lamp B) used for excitation. (e) Inside view of the measuring chamber revealing the pipetting robot and the holder for the 96-well plate.

instance, be used to assess the average mitochondrial object length (Le), width (Wi), F, margination (Ma) and TMRM fluorescence intensity (Dm).

The RAW calcein image (**Fig. 5a**; middle panel of upper row) is first processed using the rolling ball algorithm (using an empirically determined feature width of 140) to obtain a background image (**Fig. 1a**; lower row). The COR image is then obtained by subtracting the background image from the RAW image. The latter is thresholded (T value set to 40; **Supplementary Fig. 1**), resulting in the BIN image. Like the TMRM images, the calcein COR and BIN images were combined to obtain a calcein MSK image. The MSK image (**Fig. 5a**; middle panel of lower row) is used for descriptor extraction.

The RAW Hoechst image (**Fig. 5a**; right panel of upper row) was first thresholded (T) to obtain a binary image (using an

empirically determined cutoff grayvalue of 500; **Fig. 1b**). This image was subsequently filtered by applying a 7×7 MED filter (1 pass). The resulting BIN image is then subjected to a watershed-split operation (WS) to separate nuclear objects that are touching. The WS image (**Fig. 5a**; right panel of lower row) is used for descriptor extraction.

Control cell lines and replicates. The cell lines to be compared and experimental conditions should be part of the same plate (**Fig. 4**; ref. 63). The well replicates are oriented from the top to the bottom of the plate (columns) to make sure that replicates of the same cell line and/or condition are acquired with the same time delay during ZIG-ZAG scanning. In a typical experiment, eight replicates (i.e., one column of 8 wells) are performed per plate (technical replicate) in at least three different plates from

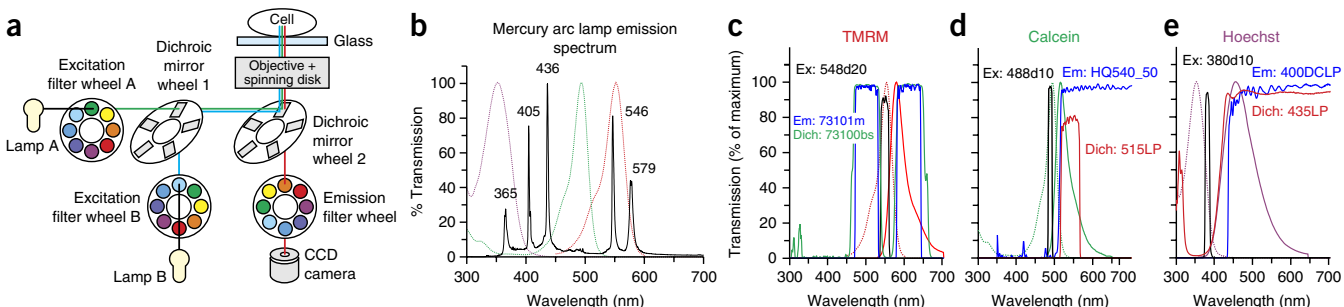
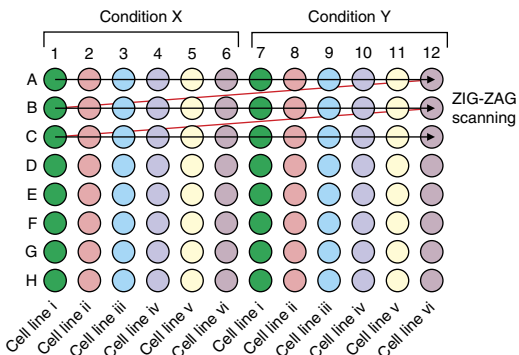


Figure 3 | Microscopy light path and spectral properties of the excitation source and filters. (a) Light path and filter configuration of the BD Pathway 855 system (see main text for details). (b) Emission spectrum of the mercury arc lamps used for excitation (black curve). Numerals indicate peak wavelengths, and dotted lines represent the excitation spectrum of TMRM (red), calcein (green) and Hoechst (purple). (c) The filter configuration used for TMRM. (d) The filter configuration used for calcein. (e) The filter configuration used for Hoechst. Information for this figure was obtained from <http://www.bd biosciences.com> (a), <http://searchlight.semrock.com> (b), <http://www.lifetechnologies.com> (b-e) and <http://www.chroma.com> (c-e).

Figure 4 | Layout of the 96-well plate and image acquisition strategy. Typical layout of the 96-well plate, allowing analysis of six different cell lines (i–vi) under two experimental conditions (X and Y). Images from individual wells are acquired, starting at the top left of the plate (well A1) and moving downward toward the lower right of the plate (well H12), using ‘ZIG-ZAG’ scanning mode (i.e., once well A12 is reached, imaging continues with well B1 and so on).

three different cell cultures (biological replicates). Technical variation can arise from (combined) errors in reagent preparation, concentration changes due to solvent evaporation, anomalies in liquid handling, pipetting errors and pipette malfunction, variations in incubation times, temperature differences and plate imaging artifacts (column effects, border effects). Biological variation can be considered an intrinsic property of living cells but might also be related to the cell system used. In the case of PHSFs⁶⁴, it is well established that growth and biological characteristics change at high passage number and high cell density (even occurring in the culture flask before seeding the cells on the 96-well plates). In our experience, an absolute minimum of 24 wells need to be imaged for each individual condition (i.e., 8 wells in three



different plates). At least one previously characterized (control) cell line should be present on each plate to allow normalization, plate-to-plate comparison and detection of anomalies⁶³. As a rule of thumb, we established, by manual analysis of rhodamine 123-, TMRM- and mtFP-stained cells^{7,19–23}, that a typical primary human fibroblast cell line from a healthy volunteer (CT5120) displays key descriptor values between 3 and 6 (*F*), 2 and 3 (*AR*) and 50 and 150 (number of mitochondria per cell; *Nc*). Once it is established that the descriptor values of the control are within these previously established boundaries, it can be used for

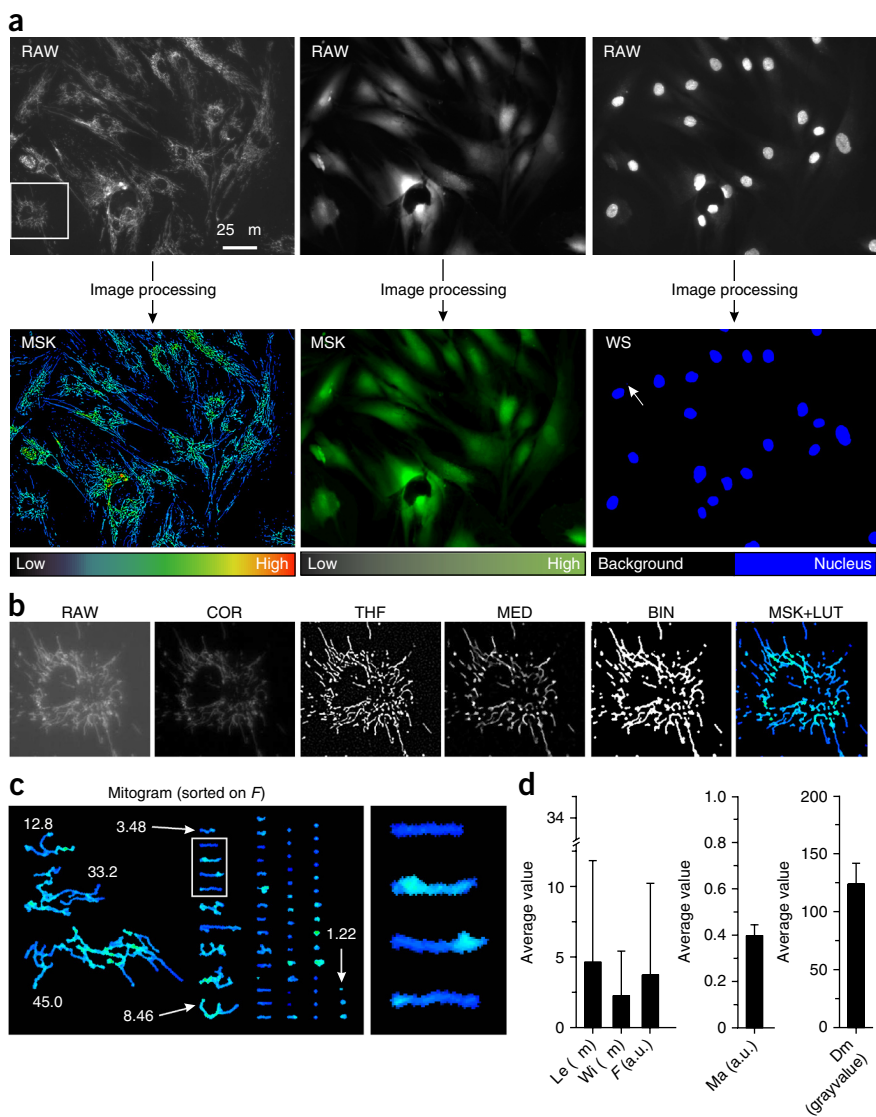


Figure 5 | Overall image quantification strategy.

(a) Upper row: typical example of a 16-bit TMRM, calcine and Hoechst image obtained from the same well (RAW images; grayvalue range: 0–65,535). For visualization purposes, grayvalues between 0 and 700 are depicted. Lower row: images obtained after image processing. (b) Illustration of the TMRM image processing pipeline for the cell highlighted (box) in a (see main text for details). (c) Mitogram calculated from the MSK+LUT image in b. Mitochondrial objects are depicted according to their formfactor (*F*) (left panel) reflecting the degree of mitochondrial length and degree of branching. Numerals indicate the *F* value of the various mitochondrial objects. The colors reflect the intensity of the TMRM fluorescence signal, ranging between low (black background) and high (green). The magnification (white box and right panel) shows four individual mitochondrial objects to illustrate heterogeneous TMRM fluorescence. (d) Average value of five descriptors (Table 1) calculated for the 61 objects in the MSK+LUT image in b. Descriptors are mitochondrial length (*Le*), mitochondrial width (*Wi*), mitochondrial formfactor (*F*), margination (*Ma*) and average mitochondrial TMRM intensity (*Dm*). Spatial descriptors (obtained in pixel units) were calibrated (to micrometers) using a pixel size of 0.157 $\mu\text{m}/\text{pixel}$. Bars represent standard deviation. BIN, binary image; COR, background-corrected image; MED, median-filtered image; MSK, masked image; RAW, image directly from microscope; LUT, look-up table; THF, top-hat filter; WS, image after watershed-split operation.

Box 1 | Median and top-hat spatial filtering

Spatial filtering^{62,73}: The properties of a spatial filter are given by a square $N \times N$ matrix of numbers (‘kernel’), which operates on pixels in the image. Because the value of N is uneven, this means that each filter kernel has a center ‘pixel’. For instance, a 3×3 filter kernel h and a (partial) 3×3 image I (with the numbers indicating pixel intensity) could be

$$h = \begin{bmatrix} 0 & -1 & 1 \\ 0 & 2 & 1 \\ 1 & 2 & 3 \end{bmatrix} \quad I = \begin{bmatrix} 1 & 0 & 1 \\ 1 & 3 & 0 \\ 1 & 2 & 2 \end{bmatrix}$$

The result of applying the spatial filter h on the image I will be calculated as follows:

1. Each pixel in the image I is multiplied by the corresponding element in the kernel h :

$$0 \times 1 + (-1) \times 0 + 1 \times 1 + 0 \times 1 + 2 \times 3 + 1 \times 0 + 1 \times 1 + 2 \times 2 + 3 \times 2 = 18$$

2. The result of this multiplication is divided by the sum of the kernel h : $18/(0 - 1 + 1 + 0 + 2 + 1 + 1 + 2 + 3) = 2$

3. The result is scaled and boosted (facultative).

4. The center pixel in the original image (i.e., 3) is replaced by its filtered value (i.e., 2)

In practice, images are much larger than 3×3 pixels, and the kernel is moved across the image to process each pixel. Importantly, the new (filtered) value of each pixel is calculated from its original (unfiltered) value.

The median filter (MED): the median filter replaces the center pixel with the median value in its neighborhood, thereby removing noise from an image. For instance, for the 3×3 image above, the pixel values can be ranked from low to high as follows: 0 – 0 – 1 – 1 – 1 – 2 – 2 – 3. The central (median) value of this sequence equals 1, meaning that the original pixel value of 3 is replaced by 1. The median filter can be applied multiple times (‘passes’), thereby amplifying its effect with each pass (**Supplementary Fig. 6A**). For effective use, the kernel size of the median filter should be smaller than that of the objects that need to be retained in the image (**Supplementary Fig. 6A**).

The top-hat filter (THF): This filter is suited for isolation of bright objects from a dark background²⁴. Its 7×7 kernel h is

$$h = \begin{bmatrix} 0 & 0 & -1 & -1 & -1 & 0 & 0 \\ 0 & -1 & -1 & -1 & -1 & -1 & 0 \\ -1 & -1 & 3 & 3 & 3 & -1 & -1 \\ -1 & -1 & 3 & 4 & 3 & -1 & -1 \\ -1 & -1 & 3 & 3 & 3 & -1 & -1 \\ 0 & -1 & -1 & -1 & -1 & -1 & 0 \\ 0 & 0 & -1 & -1 & -1 & 0 & 0 \end{bmatrix}$$

Like the median filter, the top-hat filter can be applied multiple times (passes), which amplifies its effect with each pass (**Supplementary Fig. 6B**). The ‘strength’ of the top-hat filter can be varied from 1 to 10, and this determines how much of the filtering effect is applied to the image (**Supplementary Fig. 6B**). A value of 10 specifies that the full strength (100%) of the filtered result should be applied to each pixel. Values below 10 reduce the weight of the filter—i.e., a value of 1 indicates that only 10% of the difference between the filtered pixel value and the original pixel value is applied. For effective use, the kernel size of the top-hat filter should be larger than that of the objects that need to be retained in the image (**Supplementary Fig. 6B**).

intraplate normalization of descriptor values for the other cell lines and experimental conditions (**Fig. 1c**).

Data analysis and quality control (QC) In this protocol, we apply PCA, which simultaneously considers all variables in a multidimensional space^{8,26,65}, to analyze the obtained data set. PCA is a mathematical technique that reduces the dimensionality of the data while retaining most of the variation in the data set, thereby facilitating graphic visualization⁶⁵ and explorative data analysis⁶⁶. Dimensionality reduction is achieved by identifying directions, called PCs, along which the variation in the data is maximal. The sum of variation accounted for by each PC determines how many PCs are required to faithfully represent the data set^{67,68}. There are several ‘rules’ for determining

the number of PCs to include, such as ‘Kaiser’s stopping rule’ and the ‘Scree test’⁶⁹. In our experience, two PCs suffice to allow proper multivariate analysis and QC for the type of data generated in this protocol. Alternatively, other multivariate approaches, including cluster analysis and machine learning²⁷, can be applied⁶⁵. Data analysis and quality control can be performed using the supplied MATLAB code in the m-file Iannetti_MATLAB.m (**Table 2** and the **Supplementary Software**), which carries out the following operations:

- It imports the numerical data generated by IPP into MATLAB.
- It calculates the derived descriptors (i.e., descriptor 39 to 44; see **Table 1**).
- It normalizes the data.

- It performs a PCA and creates a PCA graph and boxplot graph to visualize the data.
- It performs a QC step, to identify and remove outliers (i.e., individual wells) from the data set.
- It performs a second PCA after removal of the outliers (generates ‘cleaned data’).

- It calculates the 95% confidence ellipses of the ‘cleaned’ PCA data.
- It generates a PCA graph for visualization of the cleaned data and its 95% confidence ellipses.

Technical details related to the above operations are embedded in the Iannetti_MATLAB.m file.

MATERIALS

REAGENTS

- Suitable cells of interest. The procedure below is optimized for PHSFs taken from human skin biopsies **! CAUTION** Take the necessary precautions when working with human samples. They should be handled in a biological safety cabinet. Experiments with human cell lines must adhere to the relevant local institutional and governmental regulations and generally require informed consent.
- Medium 199 with HEPES and Phenol Red (Invitrogen, cat. no. 12340-030)
- Medium 199 without HEPES and Phenol Red (Invitrogen, cat. no. 11043-023)
- FBS (Greiner Bio-One, cat. no. 758093)
- Penicillin–streptomycin solution, 100× (Corning, cat. no. 30-002-CI)
- HEPES (1 M; Invitrogen, cat. no. 15630-08)
- DMSO (MW = 78.134 g/mol; CAS: 67-68-5; Sigma-Aldrich, cat. no. D5879-100ML) **! CAUTION** DMSO is skin-permeable and irritating.
- Trypsin–EDTA (0.5% (wt/vol)) solution, without Phenol Red, 10× concentrated (Gibco/Life Technologies, cat. no. 15400-054). Store the solution between –5 and –20 °C for up to 18 months
- PBS (pH 7.2; Gibco/Life Technologies, cat. no. 20012-068)
- Tetramethyl rhodamine methyl ester (TMRM; MW = 500.93 g/mol; CAS: 115532-50-8; Invitrogen, cat. no. T668)
- Calcein–AM (MW = 622.53 g/mol; CAS: 154071-48-4; Ebioscience, cat. no. 65-0853-39)
- Hoechst 33258 (MW = 533.88 g/mol; CAS: 23491-45-4; Invitrogen, cat. no. 94406) **! CAUTION** Hoechst stains are known mutagens and should be handled with care. The dye must be disposed of safely and in accordance with applicable regulations.

EQUIPMENT

- Culture flasks (Greiner Bio-One): 75 cm² (cat. no. 658170) and 175 cm² (cat. no. 661160)
- Centrifuge tubes (Greiner Bio-One): 15 ml (cat. no. 188271) and 50 ml (cat. no. 227261)
- Reagent reservoir (35 ml; Greiner Bio-One, cat. no. 9103006)
- Polystyrene 96-well cell culture microplates (μClear/black; working volume: 25–340 μl; total well volume: 392 μl; growth area per well 34 mm²; glass thickness: 190 μm; Greiner Bio-One, cat. no. 655090)
- Cell culture flow cabinet (Model EF/S 4; Telstar Laboratory Equipment)
- Incubator for cell culture (Heracell 150i; Thermo Fisher Scientific)
- Water bath (Model 1003; GFL)
- Neubauer hemocytometer (Hausser Scientific)
- Multi-(12-)channel pipette (Model m300; Biohit/Sartorius)

Microscopes

- An inverted microscope for cell culture (Model DM IL; Leica Microsystems)

- An automated multiwell fluorescence microscope with environmental (CO₂ and temperature) controls: Pathway 855 High-content Bioimager (Becton Dickinson). This system features two mercury arc lamps A and B (Becton Dickinson, cat. no. 341032)

Computing hardware and software

- A PC workstation (Windows 7 Pro 64-bit; Dell T7500; Xeon E5620 2.40 GHz; 24 GB RAM, Nvidia Quadro 2000; Dell Computer Corp.)
- MATLAB 8.2.0.701 (R2013b; The MathWorks)
- MATLAB Statistics Toolbox 8.3 (R2013b; The MathWorks)
- Image Pro Plus 6.3 (IPP; Media Cybernetics)
- Microsoft Excel (Microsoft Office 2010, Microsoft)
- Origin Pro 2015 (OriginLab Corp.)

REAGENT SETUP

Culture medium Medium 199 (M199) is used for cell culture, and it contains HEPES and Phenol Red. This medium should be supplemented with 10% (vol/vol) FCS, 100 IU/ml penicillin and 100 IU/ml streptomycin. The solution should be stored at 4 °C in the dark and used within 1 month after preparation. The complete formulation of this medium is provided in **Supplementary Table 2**.

Assay medium This is based on a special variant of the culture medium (M199) that does not contain Phenol Red or HEPES. This medium should be supplemented with 25 mM HEPES and is used for diluting the fluorescent probes and for washing the cells. The assay medium should be stored at 4 °C in the dark and used within 1 month after preparation. The complete formulation of this medium is provided in **Supplementary Table 2**.

TMRM stock (500 μM) TMRM is provided as a lyophilized off-white powder (25 mg) that should be protected from light/moisture and stored at –20 °C. The solid should be dissolved in dry (water-free) DMSO from a freshly opened bottle to prepare a TMRM stock solution of 500 μM. This solution should be divided into 10-μl aliquots, which should be stored at –20 °C in the dark. Each aliquot should be freshly thawed and used only once to avoid repeated freezing and thawing. The TMRM stock solution can be used for at least a year.

Calcein–AM stock (5 mM) Calcein–AM is provided as a lyophilized off-white solid (typically in 20 × 50-μg batches). It should be shielded from light/moisture and stored at –20 °C. The solid should be dissolved in dry (water-free) DMSO from a freshly opened bottle, yielding a stock solution of 5 mM. This solution should be divided in 10-μl aliquots, which should be stored at –20 °C in the dark. Each aliquot should be used while fresh and discarded after use to avoid repeated freezing and thawing. The calcein–AM stock solution can be used for at least a year.

Hoechst 33258 stock (1 mg/ml) Hoechst 33258 is delivered as a 1 mg/ml stock solution in water (1.87 mM), and it should be stored at 2–8 °C in the dark. The Hoechst 33258 stock solution can be used for at least a year.

PROCEDURE

Seeding of the cells on a 96-well plate ● TIMING ~90 min/plate

- 1| Wash the cells twice with 1× PBS.
- 2| Add an adequate volume of 1× Trypsin–EDTA (diluted in PBS) to cover the cell-containing surface of the culture flask (typically 1 ml for a T75 culture flask), and incubate it for 5 min (37 °C, 5% (wt/vol) CO₂).
- 3| Resuspend the cells in assay medium prewarmed to 37 °C (typically by adding 9 ml of medium for a T75 culture flask).
- 4| Perform a thorough cell count using a cell counting chamber or Coulter counter.

PROTOCOL

5| Resuspend the cells and seed the cells into a 96-well plate so that each well contains 2,000–3,000 cells in 100 µl of culture medium. Culture the cells for 24 h (37 °C, 5% (wt/vol) CO₂) to reach a final confluence of 50–60%. The number of cells to be seeded to reach this confluence generally differs per cell line or type, and it needs to be empirically determined. For a typical cell seeding example, see **Figure 4**.

▲ **CRITICAL STEP** Reaching a correct level of cell confluence after 24 h (illustrated in **Supplementary Fig. 2**) is crucial for reliable image quantification.

? TROUBLESHOOTING

Cell staining and imaging ● **TIMING** ~90 min/plate

6| 1 h before image acquisition, set the temperature (to 37 °C) and the CO₂ control (to 5%), and turn on lamps A and B (excitation sources) of the microscope.

7| Mount the 40× objective on the microscope and allow it to thermally equilibrate.

8| Prewarm the assay medium to 37 °C in a water bath.

9| Prepare a 250 nM TMRM ‘loading solution’ by diluting the 500 µM TMRM stock solution in the prewarmed assay medium. Take care that the final DMSO concentration in the loading solution does not exceed 0.1% (vol/vol). Use the same TMRM loading solution for all plates measured on the same day to reduce technical variation.

10| To start TMRM staining, add 20 µl of the TMRM loading solution from Step 9 (250 nM) to each well using the 12-channel pipette. This yields a final TMRM concentration of 50 nM.

▲ **CRITICAL STEP** Because of evaporation, the total volume of culture medium in each well will be reduced. We empirically established that only 80 µl of the initial 100 µl of culture medium is left in each well after 24 h of cell culture. There was no substantial difference in TMRM intensity, calcein intensity or Hoechst intensity between the wells at the outer rim and those in the central part of the plate.

11| Carefully check whether the volume of TMRM loading solution in each pipette tip is correct (air bubbles should be absent) before pipetting.

12| To mix, gently pipette up and down four times after addition of the TMRM loading solution.

13| Incubate the cells for 30 min at 37 °C, 5% CO₂.

14| During the cells’ incubation with TMRM, prepare a loading solution containing a 5 µM final concentration of calcein and a 1.5 µg/ml final concentration of Hoechst in prewarmed assay medium. Use the same calcein/Hoechst loading solution for all plates measured on the same day to reduce technical variation.

15| After the 30-min TMRM incubation, add 100 µl of the calcein/Hoechst loading solution to each well using the 12-channel pipette, without washing or mixing. Add the calcein/Hoechst loading solution at the edge of each well (so not directly on top of the cells), holding the pipette horizontal. Addition of the calcein/Hoechst loading solution dilutes the extracellular TMRM concentration, which is required for signal stability (**Supplementary Fig. 3**). The final extracellular concentrations should now equal 25 nM (TMRM), 2.5 µM (calcein) and 0.75 µg/ml (Hoechst).

16| Place the 96-well plate in the BD Pathway 855 measuring chamber, and manually focus on a random well. (For this microscopy system, typically a Z-position value near 5,200 is required.) Start the TMRM image acquisition using a predefined macro (full macro settings are provided in **Supplementary Table 3**). This acquisition will take 15 min. Next, keep the plate inside the measuring chamber and incubate for another 5 min to complete the calcein/Hoechst staining (20 min in total will have passed after completion of Step 15).

? TROUBLESHOOTING

17| Discard the TMRM/calcein/Hoechst-containing medium by turning the plate upside down in a single fluid motion.

18| Gently wash each well in the plate 2 times (12-channel pipette) with 100 µl of assay medium. This will remove extracellular calcein, which would otherwise induce a continuous increase in calcein signal over time.

19| Pipette 100 µl of assay medium into each well (12-channel pipette).

20 Start the calcein/Hoechst image acquisition (this will take 20 min).

? TROUBLESHOOTING

■ **PAUSE POINT** Images are automatically saved on the microscope computer; the rest of the protocol can be carried out at any moment later in time.

Image processing and descriptor extraction with IPP ● TIMING ~30 min/plate

▲ **CRITICAL** For this part of the protocol, as well as the next section, we provide tutorial data files (**Supplementary Software**). The .zip file needs to be copied onto a hard-drive and extracted, yielding a directory named \Tutorial\, the contents of which are given in **Table 2**. Processing and quantification of the RAW images, as visualized in the flowchart (**Fig. 1b**), is performed by a single IPP Basic script (Iannetti_IPP.bas) that automatically carries out the various image processing described in the ‘Image processing and descriptor extraction’ section by applying built-in IPP functions. Further technical details related to the image processing and descriptor extraction code are embedded within the Iannetti_IPP.bas file. Typical results obtained in this section are shown in **Figure 6**.

21 Start the IPP software.

22 Load the Iannetti_IPP.bas script. To do this, click ‘Macro’ > ‘Macro’ > ‘Change’, select ‘Iannetti_IPP.bas’ and click ‘Open’ > ‘OK’. The Macro menu now contains the following six items: TMRM_Processing, TMRM_DescriptorExtraction, Calcein_Processing, Calcein_DescriptorExtraction, Hoechst_Processing and Hoechst_DescriptorExtraction.

TABLE 2 | Processing scripts and tutorial data files.

File name	Content of file
Files for image processing and extraction with IPP (directory: \Tutorial\IPP_processing_analysis\)	
Iannetti_IPP.bas	IPP script for image processing and quantification
RAW_TMRM.tif	RAW 16-bit TMRM image directly from the microscope (TIFF format)
RAW_Calcein.tif	RAW 16-bit calcein image directly from the microscope (TIFF format)
RAW_Hoechst.tif	RAW 16-bit Hoechst image directly from the microscope (TIFF format)
TMRM.cnt	Numerical data file: quantification data for the RAW_TMRM.tif image
Calcein.cnt	Numerical data file: quantification data for the RAW_Calcein.tif image
Hoechst.cnt	Numerical data file: quantification data for the RAW_Hoechst.tif image
Files for data visualization and QC with MATLAB (directory: \Tutorial\MATLAB_QC\)	
Iannetti_MATLAB.m	MATLAB m-file that performs the PCA and QC
auto.m	MATLAB m-file used by Iannetti_MATLAB.m
ellipses.m	MATLAB m-file used by Iannetti_MATLAB.m
import_cnt.m	MATLAB m-file used by Iannetti_MATLAB.m
headers.mat	MATLAB MAT-file used by Iannetti_MATLAB.m
ConditionX_ci.cii_TMRM.cnt	Numerical data file: TMRM quantification data for cell lines 1 and 2 (condition X)
ConditionX_ci.cii_Calcein.cnt	Numerical data file: calcein quantification data for cell lines 1 and 2 (condition X)
ConditionX_ci.cii_Hoechst.cnt	Numerical data file: Hoechst quantification data for cell lines 1 and 2 (condition X)
ConditionY_ci.cii_TMRM.cnt	Numerical data file: TMRM quantification data for cell lines 1 and 2 (condition Y)
ConditionY_ci.cii_Calcein.cnt	Numerical data file: calcein quantification data for cell lines 1 and 2 (condition Y)
ConditionY_ci.cii_Hoechst.cnt	Numerical data file: Hoechst quantification data for cell lines 1 and 2 (condition Y)
Other files (directory: \Tutorial\)	
DataExtraction.xlsx	Excel file that automatically extracts descriptor values from a .cnt file

PROTOCOL

23 | The provided IPP script assumes a fixed directory for data storage. In the provided code, this is c:\Users\Khondrion\Desktop\cnt\ Adjust the script to your working directory, changing the below code. Click ‘Macro’ > ‘Macro’ > ‘Edit’ and replace the directory name with your working directory:

In the section ‘Sub TMRM_DescriptorExtraction’, change the line

```
"ret = IpBlbSaveData ("C:\Users\Khondrion\Desktop\cnt\...",
```

In the section ‘Sub Calcein_DescriptorExtraction’, change the line

```
"ret = IpBlbSaveData ("C:\Users\Khondrion\Desktop\cnt..."
```

In the section ‘Sub Hoechst_DescriptorExtraction’, change the line

```
"ret = IpBlbSaveData (C:\Users\Khondrion\Desktop\cnt..."
```

24 | Save the script with the new working directory by clicking ‘File’ > ‘Save’.

25 | Load the provided TMRM example image into IPP. To do this, click ‘Sequence’ > ‘Merge files...’, select ‘RAW_TMRM.tif’ and click ‘Open’. The figure should appear as in **Figure 6a**.

▲ **CRITICAL STEP** The IPP macro was designed to also operate on a sequence of multiple images (i.e., obtained from a 96-well plate; not provided here). To use the IPP macro on an image sequence, this first needs to be created by using the ‘Sequence’ > ‘Merge files’ menu option in IPP, followed by selection of the first and last image and clicking ‘Open’.

26 | Perform the image processing of the ‘RAW_TMRM.tif image’, by clicking ‘Macro’ > ‘TMRM_Processing’. This creates the BIN image (**Fig. 6b**) and an MSK image (**Fig. 6c**).

TROUBLESHOOTING

27 | Perform the image quantification by clicking on the MSK image, and then click ‘Macro’ > ‘TMRM_DescriptorExtraction’. The quantified individual mitochondrial objects are now highlighted by a red outline (**Fig. 6d**), and the numerical data are saved in the working directory (TMRM.cnt file).

▲ **CRITICAL STEP** For convenience, example .cnt files have been included in the **Supplementary Software**. These files should be moved from the Tutorial\IPP_processing_analysis\ directory to another directory before re-executing Step 27 to prevent them being overwritten.

28 | Repeat Steps 25 to 27 to process and quantify the provided Calcein.tif and Hoechst.tif images to obtain the Calcein.cnt and Hoechst.cnt files

▲ **CRITICAL STEP** For each 96-well plate, descriptor data are stored in three files: TMRM.cnt (33 descriptors of interest), Calcein.cnt (2 descriptors of interest) and Hoechst.cnt (3 descriptors of interest). These files can be opened and further processed/analyzed/visualized using Excel, MATLAB, Origin Pro or other data analysis software. We provide an Excel file (DataExtraction.xlsxm) in the **Supplementary Software** for easy inspection of the .cnt files and extraction of numerical values for specific descriptors by drag-and-drop.

■ **PAUSE POINT** After generation of the .cnt files, the remainder of the protocol can be carried out at a later time.

Data visualization and QC with MATLAB ● TIMING

~15 min/plate

▲ **CRITICAL** To illustrate this part of the protocol, we provided the .cnt files for a larger data set obtained from a 96-well plate (**Table 2**). In this experiment, we aimed to quantify mitochondrial morphofunction in two primary human fibroblast cell lines (1 and 2) that were cultured under two experimental conditions (X and Y). In this example, 48 wells were measured for each condition (i.e., 16 wells in three independent experiments/plates). Importantly, optimal

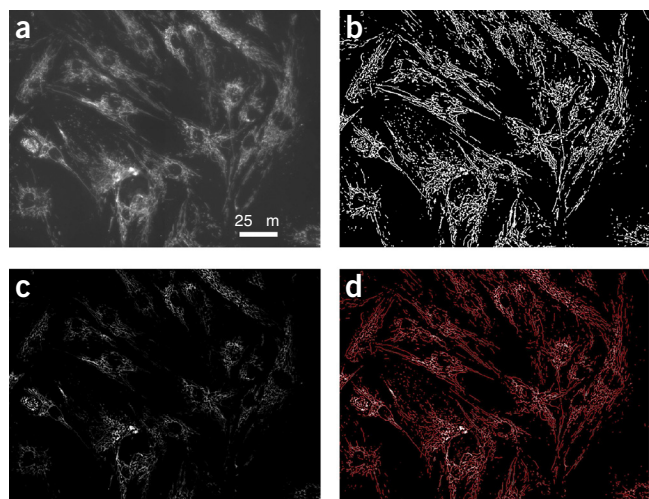


Figure 6 | Image processing of the TMRM image. (a) The RAW_TMRM.tif image. (b) The BIN image calculated from the RAW_TMRM.tif image. (c) The MSK image calculated from the RAW_TMRM.tif image. (d) Highlighted mitochondrial objects (red outlines) that are quantified.

results required a plate layout compatible with **Figure 4**, in which both cell lines were measured under both conditions in the same plate. Cell line 1 was used as a control, and the average descriptor values obtained with this cell line were used to normalize the data for cell line 2 on the same day/plate.

29 Start the MATLAB software. Before performing the MATLAB analysis, the relevant files from the **Supplementary Software** (see 'Files for data visualization and QC with MATLAB' in **Table 2**) have to be present in the same directory. If other file names are required, they can be manually changed in the Iannetti_MATLAB.m file (line 53–59).

30 If it is not open yet, activate the Current Folder window by clicking /Desktop/Current Folder/ and navigate to the folder containing the tutorial files above.

31 Execute the file Iannetti_MATLAB.m by right-clicking on its filename and clicking /Run. In the MATLAB command window, the following instruction appears: 'Specify the condition you want to analyse:'

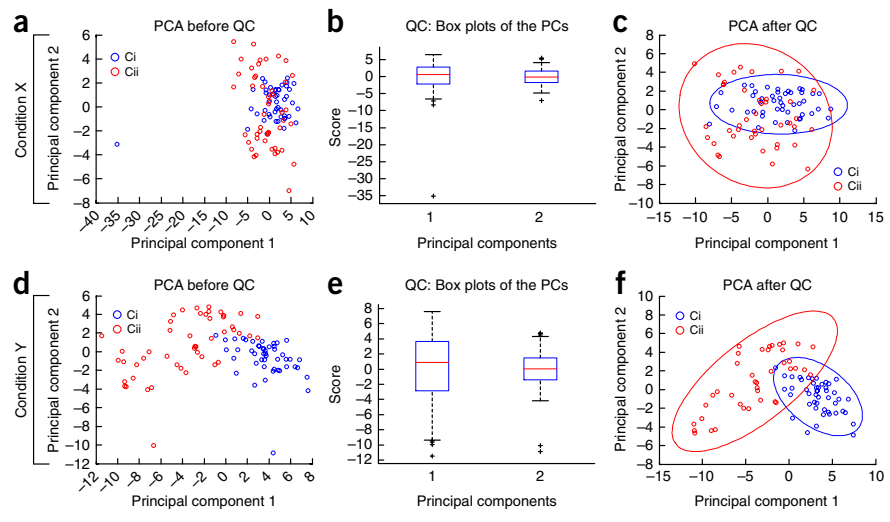
32 Perform the analysis for condition X (by typing 'x' followed by Enter) or condition Y (by typing 'y' followed by Enter). This process will take ~50 s. For both conditions X and Y (run the Iannetti_MATLAB.m file twice), MATLAB will generate three figures (**Fig. 7**). The first figure contains the result of the PCA visualized by plotting principal component 1 (PC1; x axis) versus principal component 2 (PC2; y axis) before the QC (**Fig. 7a,d**). The second figure contains a box-plot of PC1 and PC2 revealing the outliers (QC; **Fig. 7b,e**). The third figure contains the result of the PCA analysis visualized by plotting PC1 versus PC2 with the outliers removed (**Fig. 7c,f**). In our experience, visual inspection of the images revealed that such outliers (e.g., condition X: well 54 and condition Y: well 13) displayed aberrant staining (**Fig. 8a**).

TROUBLESHOOTING

The presented protocol was specifically developed for quantitative analysis of mitochondrial morphology, $\Delta\psi$ and cellular/nuclear parameters in PHSFs using 96-well plates. To this end, we used a combined staining of TMRM/calcein/Hoechst, which was imaged using a BD Pathway 855 microscopy system. However, our strategy is compatible with any microscopy system that features an environmental control system, allows automated image acquisition and meets the spectral requirements (excitation, emission) for combined and specific imaging of TMRM, calcein and Hoechst. For successful implementation of the protocol, one needs to establish the following (see also **Supplementary Figs. 2–5**):

- The PHSFs are viable when cultured on multiwell plates and are firmly attached.
- The cell density (confluence) is appropriate (**Supplementary Fig. 2**).
- Each well is properly mixed after TMRM addition (**Supplementary Fig. 3**).
- TMRM photobleaching during image acquisition is absent or does not interfere with descriptor extraction (**Supplementary Fig. 3**).
- The automatically acquired images are in focus (**Supplementary Fig. 4**).
- TMRM autoquenching is absent (**Supplementary Fig. 5**).
- The TMRM signal is able to report both $\Delta\psi$ depolarization and hyperpolarization (**Supplementary Fig. 5**).

Figure 7 | Descriptor extraction, data visualization and QC procedure. (a) Graphical output of the MATLAB analysis. PCA for all wells under experimental condition X. Each symbol corresponds to an individual well for cell line 1 ('Ci', blue symbols) or cell line 2 ('Cii', red symbols). (b) Detection of outlier wells (crosses) in the PCA of **a** using a boxplot analysis of principal component 1 (PC1) and 2 (PC2) for condition X. Box-plot settings: the top and bottom of each box reflects the 25th and 75th percentile, respectively. The median value is indicated by a horizontal red line within the box. The error bars ('whiskers') extend to the furthest observations within the whisker length, which was set at 1.0-times the interquartile range. Observations outside the whiskers were considered outliers (marked by '+'). (c) Same as **a**, but now the outlier wells that were detected in **b** have been removed. This panel demonstrates that cell lines 1 and 2 are similar under experimental condition X. (d) Same as **a**, but now showing analysis for experimental condition Y. (e) Same as **b**, but now showing analysis for experimental condition Y. (f) Same as **c**, but now showing analysis for experimental condition Y. In the latter condition, cell lines 1 and 2 are dissimilar.



PROTOCOL

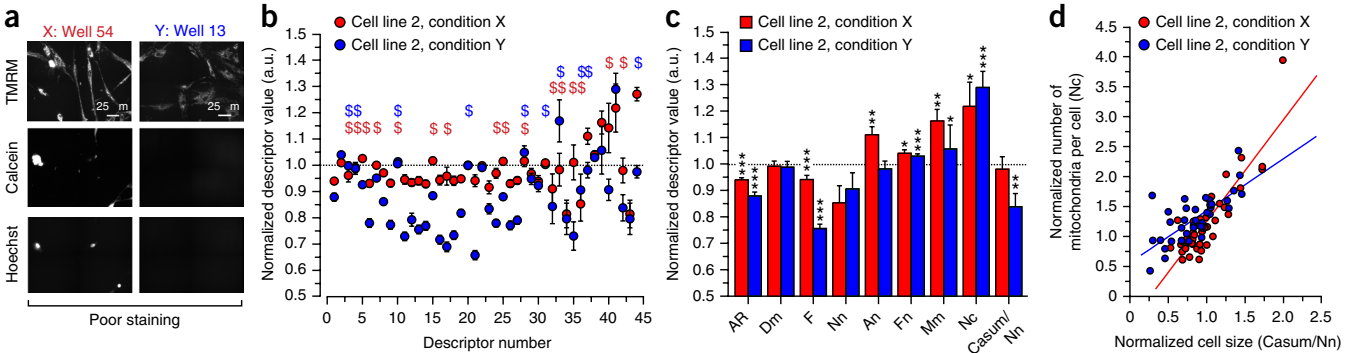


Figure 8 | Quality control and monovariate and bivariate data visualization. Two cell lines (1 and 2) were cultured under two experimental conditions (X and Y) on three different plates using the plate layout in **Figure 4**. (a) Examples of staining aberrations detected by the analysis in **Figure 7b,e** (condition X: well 54 and condition Y: well 13). (b) Average normalized values of the 44 descriptors in **Table 2** for cell line 2 cultured under experimental conditions X (red) and Y (blue). The data were normalized on the average value obtained for cell line 1 on the same day/plate (i.e., cell line 1 is characterized by a y value of 1.0, marked by the horizontal dotted line). Statistical analysis revealed that the marked descriptors (\$) for cell line 2 did not significantly differ ($P > 0.05$) from cell line 1 in condition X (red symbols) or condition Y (blue symbols). (c) Average values of a selected subset of ‘biologically meaningful’ descriptors for cell line 2 cultured under experimental condition X (red) and condition Y (blue). The data were normalized on the average value obtained for cell line 1 on the same day/plate (dotted line). Statistical analysis revealed significant differences between various descriptors. (d) Example of a bivariate analysis using the number of mitochondria per cell (Nc; y axis) and cell size (Casum/Nn; x axis) for cell line 2 cultured under experimental condition X (red) and condition Y (blue). Both descriptors were normalized on the average value obtained for cell line 1 on the same day/plate. A linear fit to the data revealed that Nc increases with Casum/Nn (Red line: $P < 0.0001$, $R = 0.88$; Blue line: $P < 0.0001$, $R = 0.71$), demonstrating that the number of mitochondria per cell increases as a function of cell size. Statistics: mean values were compared (b,c) using an unpaired independent t-test (Bonferroni-corrected). * $P < 0.05$, ** $P < 0.01$ and *** $P < 0.001$.

With regard to TMRM staining, the most crucial part of the procedure is the dilution of the extracellular TMRM concentration following TMRM staining and before TMRM image acquisition⁷⁰. For PHSFs, the extracellular TMRM loading concentration needs to be twofold diluted to allow signal stability over time (**Supplementary Fig. 3**). This dilution factor is probably cell-type-specific. Once the cell culture and staining conditions are optimal, successful image processing and descriptor extraction requires that the acquired microscopy images display certain properties. The key part of the TMRM image processing pipeline is the generation of the BIN image, in which white mitochondrial objects are represented on a black background. Faithful calculation of the BIN image from the background-corrected TMRM image (COR) requires that the mitochondria-specific TMRM signal is high enough, that the image is relatively noise-free (i.e., contains few noise-related pixels introduced by defocusing and/or the optical/electronic systems of the microscope) and that each true mitochondrial object consists of enough pixels to avoid its erasure from the image by the median filtering (MED). In case of other cell types, the THF and MED filtering used in this protocol can be directly applied if:

- Mitochondrial TMRM signals are sufficiently above background (i.e., cytosolic, nuclear and extracellular TMRM signals).
- The acquired TMRM images are relatively noise-free.
- The cell type displays axial dimensions (‘flatness’) similar to those of PHSFs.
- The cells contain mitochondrial objects with a (pixel) size (Am) similar to that of PHSFs.

When (several of) these four criteria are not met, we strongly advise against blindly applying our protocol but instead to empirically assess whether alternative settings of the THF and MED filters might be appropriate (**Supplementary Fig. 6**). Changing these settings is often required when small cells, small mitochondrial objects in close vicinity to each other and/or cells displaying a considerable axial dimension are imaged. In these cases, 3D analysis using confocal microscopy might be an option^{15,40}. Descriptors that are particularly informative during troubleshooting include the following:

- Nn and confluence % (C%; fraction/percentage of the image covered), to detect cell densities that are too low or too high (Nn; **Supplementary Fig. 2**).
- Am, AR, F and Nc, which are collectively sensitive to defocusing or the presence of noise in the image (**Supplementary Fig. 4**).
- Descriptors such as Dstdv, which is suited to detect fluorescence saturation and the presence of objects with a very high fluorescence intensity.

Additional troubleshooting advice can be found in **Table 3**. By using the information provided in this protocol and the fully annotated IPP and MATLAB scripts, the presented image processing/quantification and data analysis/visualization strategies can be implemented with relative ease using open-source software (see Eliceiri *et al.*⁷¹ for an overview).

TABLE 3 | Troubleshooting table.

Step	Problem	Possible reason	Solution
Cell culture			
5	Cell confluence is too low	Too few cells seeded or a low proliferation rate. Error made during cell counting	Seed more cells or culture for longer time
	Cell confluence is too high	Too many cells seeded or a high proliferation rate. Error made during cell counting	Seed fewer cells or culture for shorter time
	Low cell proliferation rate	The cell passage number is too high (PHSFs; ref. 64)	Use a fresh batch of cells
		The cell confluence reached in the culture flask before seeding cells on the 96-well plate is too high	Split the cells in a new flask and allow them to recover for at least 48 hrs before 96-well plate seeding
Cell staining			
16	TMRM fluorescence is too low	TMRM is bound to medium components during the staining period, which reduces its effective concentration	Reduce the serum amount. Use a different medium
20	Calcein fluorescence is too low	The AM tail of calcein-AM is hydrolyzed before cell staining Low esterase activity in cells Calcein-AM binds to serum in the medium, thereby reducing its effective concentration Calcein-AM is actively extruded from the cell ⁶⁰	Use a fresh batch of calcein-AM. Prevent hydrolysis by aliquotting and avoiding repeated freezing and thawing Use another cell type Reduce the amount of serum. Use another serum batch. Increase the concentration of calcein-AM Block multidrug transporter, and stain at a lower temperature
Microscopy imaging			
16	TMRM intensity is not stable	Excitation intensity is too high (photobleaching) Changes in ΔV TMRM is leaking out of the mitochondria/cell TMRM is still accumulating in the cell after the staining period because of improper mixing Illumination of TMRM photoactivates mPTP opening, e.g., ref. 58	Reduce image acquisition time; reduce intensity of excitation light Quantify ΔV using electrophysiology ⁵⁴ . Use a ΔV correction technique ⁵⁵ Increase the extracellular TMRM concentration and test with FCCP Properly dilute the extracellular TMRM after the staining period by thorough mixing
16 and 20	Cells die during imaging Fluorescence image is not sharp	Excitation intensity is too high Focus drift, autofocus problem, optical misalignment Cell has considerable axial dimensions Mitochondrial objects are blurred	Reduce excitation intensity or acquire fewer images per well Allow the microscopy system to warm up before experiments. Adjust autofocus settings. Service the microscopy system Increase the time for cell attachment to glass, use CLSM imaging and analysis of single optical slices, or use 3D imaging strategy ⁴⁰ Use faster imaging. If possible, perform image acquisition at a lower temperature (e.g., 20 °C)
20	Calcein intensity is not stable	Calcein-AM is still present extracellularly and taken up by the cells	Wash the cells more thoroughly to remove extracellular calcein-AM

(continued)

PROTOCOL

TABLE 3 | Troubleshooting table (continued).

Step	Problem	Possible reason	Solution
Image processing			
26	True mitochondrial objects are erased during processing	Mitochondrial pixel size is too small The settings of the MED filter are incorrect The settings of the THF filter are incorrect	Use an objective with a higher magnification Check and/or use alternative MED filter settings Check and/or use alternative THF filter settings
	False mitochondrial objects are introduced during processing	The TMRM image is too noisy Mitochondria-specific signal is too low	Increase TMRM concentration during cell staining, increase excitation intensity during image acquisition. Use an alternative reporter molecule for mitochondrial staining (e.g., MTDR or MTR, thereby losing $\Delta\Psi$ information)

$\Delta\Psi$, mitochondrial membrane potential; ΔV , plasma membrane potential; AM, acetoxymethyl ester; CLSM, confocal laser scanning microscopy; FCCP, mitochondrial uncoupler p-trifluoromethoxy carbonyl cyanide phenyl hydrazine; MED, median spatial filter; mPTP mitochondrial permeability transition pore; MTDR, MitoTracker Deep Red; MTR, MitoTracker Red CMXROS; PHSF, primary human skin fibroblast; THF, top-hat spatial filter; TMRM, tetramethyl rhodamine methyl ester.

TIMING

Steps 1–5, seeding of the cells on a 96-well plate: ~90 min/plate

Steps 6–20, cell staining and imaging: ~90 min/plate

Steps 21–28, image processing and descriptor extraction with IPP: ~30 min/plate

Steps 29–32, data visualization and QC with MATLAB: ~15 min/plate (depends on the type of analysis)

ANTICIPATED RESULTS

After removal of the outliers, the two PCs in condition X accounted for 58% of the total variation, and in condition Y they accounted for 67% of the total variation. Visual inspection of the two scatterplots of PC1 and PC2 revealed that cell lines 1 and 2 were very similar under condition X (**Fig. 7c**); in contrast, cell lines 1 and 2 were dissimilar in condition Y (**Fig. 7f**). For statistical analysis (e.g., to determine whether the two cell lines significantly differ from each other in conditions X and Y), the centroid (average) values of PC1 and PC2 for the two cell lines under conditions X and Y can be compared. To this end, it first should be assessed whether the individual values for PC1 and PC2 are normally distributed. This was carried out by performing a Shapiro–Wilk test, which showed that the PC2 data for cell line 2 in condition Y was not normally distributed. This means that in this example a nonparametric test is required to compare the data. For independent samples, as is the case in this protocol, a Mann–Whitney or Kolmogorov–Smirnov test can be applied⁶⁵. Using the latter test, the following results were obtained for condition X (PC1: cell lines 1 and 2 are significantly different, $P = 0.00987$; PC2: cell lines 1 and 2 are significantly different, $P = 8.61\text{E-}5$) and condition Y (PC1: cell lines 1 and 2 are significantly different, $P = 8.65\text{E-}15$; PC2: cell lines 1 and 2 are significantly different, $P = 2.57\text{E-}5$). This means that cell lines 1 and 2 are better separated for condition Y, especially with respect to PC1.

After the PCA approach shown in **Figure 7**, single descriptors (univariate) were compared between cell lines 1 and 2 in conditions X and Y (**Fig. 8b**). After QC, various descriptors are suited for direct ‘biological’ interpretation¹⁵. For instance, under conditions X and Y, cell line 2 displayed a reduction in AR and F , and an increase in Nc (**Fig. 8c**). This means that the mitochondria are smaller (lower AR, F), less branched (lower F) and more abundant (increased Nc) than in control cell line 1, which is indicative of mitochondrial fragmentation. The latter was paralleled by condition-specific changes in nuclear morphology, as indicated by the alterations in An (the average nuclear size) and Fn (a measure of nuclear ‘roundness’). Moreover, an increase in mitochondrial mass (Mm; both conditions) and decrease in average cell size (Casum/Nn; condition Y) were observed. By contrast, the Dm value (a measure of average mitochondrial TMRM intensity) for cell line 2 was similar to that of cell line 1 (i.e., the normalized Dm value was close to 1). This suggests that the $\Delta\Psi$ value is similar for cell lines 1 and 2 in both conditions. In addition to comparing single descriptors, the relationship between two variables can also be informative (bivariate analysis). For example, plotting the Nc as a function of cell size (Casum/Nn) revealed a linear correlation (**Fig. 8d**). This demonstrates that larger cells contain more mitochondria⁷². For this reason, in our protocol the total number of mitochondrial objects in an image (Ot) was normalized to the total cell area in the image (Casum). In this way, a meaningful estimate of the true number of mitochondria per cell can be calculated.

Note: Any Supplementary Information and Source Data files are available in the online version of the paper.

ACKNOWLEDGMENTS This research was supported by the Marie-Curie Initial Training Networks (ITN) grant ‘MEET’ (Mitochondrial European Educational Training; FP7-PEOPLE-2012-ITN), a PM-Rare (Priority Medicines Rare Disorders and Orphan Diseases) grant from the Netherlands Organization for Health Research and Development—Medical Sciences (40-41900-98-033), the Energy4All Foundation (<http://www.energy4all.eu>) and the CSBR (Centres for Systems Biology Research) initiative from the Netherlands Organisation for Scientific Research (NWO; CSBR09/013V). We thank L. Blanchet and M. Pellegrini (both from Khondrion BV) for training, practical assistance and discussions.

AUTHOR CONTRIBUTIONS W.J.H.K. developed the original microscopy and image processing strategy on which this protocol is based. E.F.I., J.B. and W.J.H.K. designed the experiments. E.F.I. performed the experiments. E.F.I. and W.J.H.K. analyzed the data and prepared the figures. E.F.I., J.A.M.S., J.B., P.H.G.M.W. and W.J.H.K. wrote and proof-read the manuscript. W.J.H.K. supervised the research.

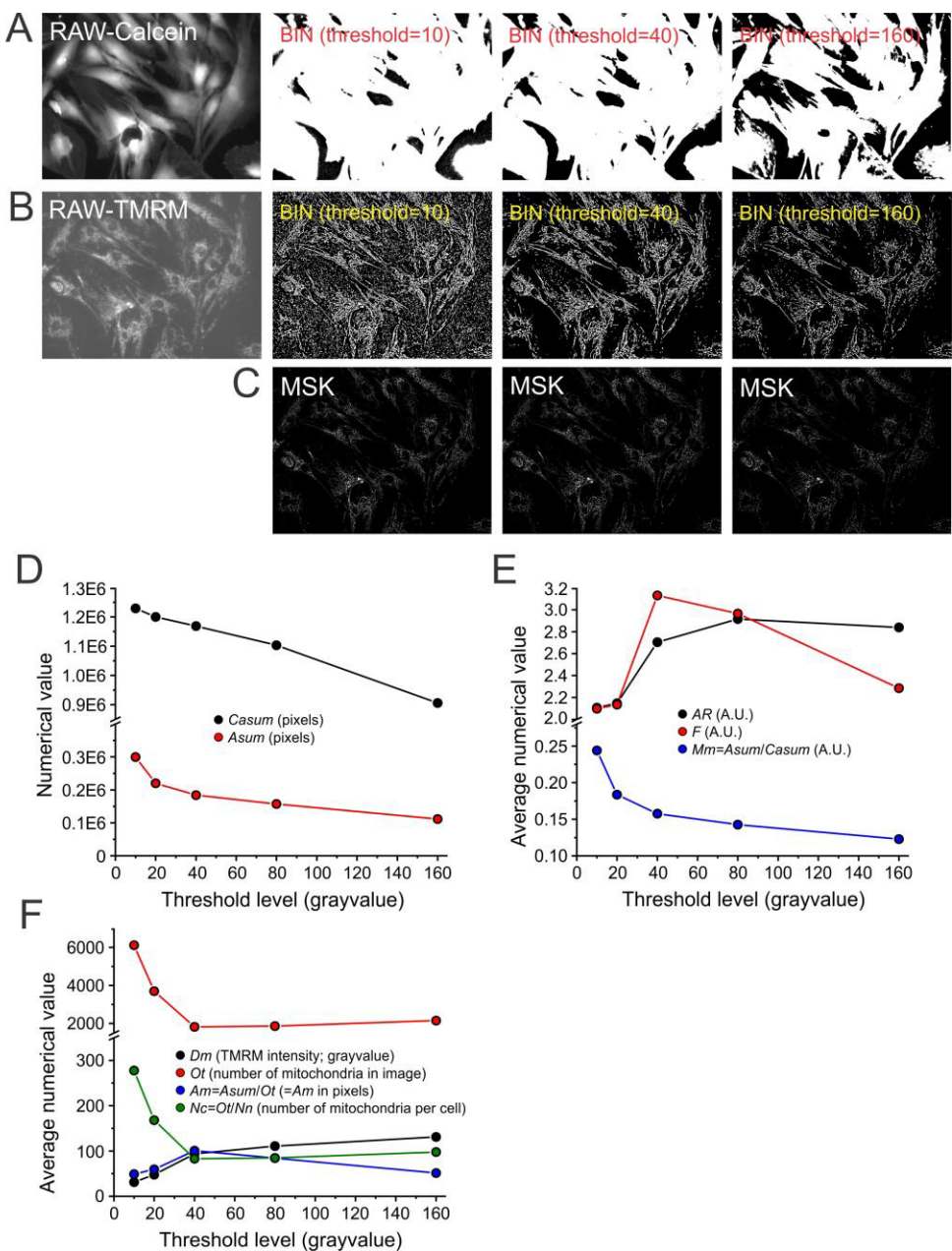
COMPETING FINANCIAL INTERESTS The authors declare competing financial interests: details are available in the online version of the paper.

Reprints and permissions information is available online at <http://www.nature.com/reprints/index.html>.

- Chandel, N.S. Mitochondria as signalling organelles. *BMC Biol.* **12**, 34 (2014).
- Westermann, B. Mitochondrial fission and fusion in cell life and death. *Nat. Rev. Mol. Cell Biol.* **11**, 872–884 (2010).
- Chan, D.C. Fusion and fission: interlinked processes critical for mitochondrial health. *Annu. Rev. Genet.* **46**, 256–287 (2012).
- Twig, G. et al. Fission and selective fusion govern mitochondrial segregation and elimination by autophagy. *EMBO J.* **27**, 433–446 (2008).
- Willems, P.H.G.M., Rossignol, R., Dieteren, C.E.J., Murphy, M.P. & Koopman, W.J.H. Redox regulation and mitochondrial dynamics. *Cell Metab.* **22**, 207–218 (2015).
- Mitchell, P. & Moyle, J. Chemosmotic hypothesis of oxidative phosphorylation. *Nature* **213**, 137–179 (1967).
- Koopman, W.J.H., Distelmaier, F., Esseling, J.J., Smeitink, J.A.M. & Willems, P.H.G.M. Computer-assisted live cell analysis of mitochondrial membrane potential, morphology and calcium handling. *Methods* **46**, 304–311 (2008).
- Iannetti, E. et al. High-content and high-throughput analysis of mitochondrial dynamics. *Int. J. Biochem. Cell Biol.* **63**, 66–70 (2015).
- Mishra, P. & Chan, D.C. Metabolic regulation of mitochondrial dynamics. *J. Cell Biol.* **212**, 379–387.
- Schrepfer, E. & Scorrano, L. Mitofusins, from mitochondria to metabolism. *Mol. Cell* **61**, 683–694 (2016).
- Toyama, E.Q. et al. AMPK-activated protein kinase mediates mitochondrial fission in response to energy stress. *Science* **351**, 275–281 (2016).
- Wai, T. & Langer, T. Mitochondrial dynamics and metabolic regulation. *Trends Endocrinol. Metab.* **27**, 105–117 (2016).
- Koopman, W.J.H., Willems, P.H.G.M. & Smeitink, J.A.M. Monogenic mitochondrial disorders. *N. Eng. J. Med.* **366**, 1132–1141 (2012).
- Koopman, W.J.H., Distelmaier, F., Smeitink, J.A.M. & Willems, P.H.G.M. OXPHOS mutations and neurodegeneration. *EMBO J.* **32**, 9–29 (2013).
- Tronstad, K.J. et al. Regulation and quantification of cellular mitochondrial morphology and content. *Curr. Pharm. Des.* **20**, 5643–5652 (2014).
- Rowland, A.A. & Voeltz, G.K. Endoplasmic reticulum-mitochondria contacts: function of the junction. *Nat. Rev. Mol. Cell Biol.* **13**, 607–625 (2012).
- Picard, M., Shirihi, O.S., Gentil, B.J. & Burelle, Y. Mitochondrial morphology transitions and functions: implications for retrograde signalling? *Am. J. Physiol. Regul. Integr. Comp. Physiol.* **304**, R393–R406 (2013).
- Koopman, W.J.H. et al. Mammalian mitochondrial complex I: biogenesis, regulation, and reactive oxygen species generation. *Antioxid. Redox Signal.* **12**, 1431–1470 (2010).
- Koopman, W.J.H. et al. Partial complex I inhibition decreases mitochondrial motility and increases matrix protein diffusion as revealed by fluorescence correlation spectroscopy. *Biochim. Biophys. Acta* **1767**, 940–947 (2007).
- Koopman, W.J.H. et al. Inhibition of complex I of the electron transport chain causes oxygen radical-mediated mitochondrial outgrowth. *Am. J. Physiol. Cell Physiol.* **288**, C1440–C1450 (2005).
- Koopman, W.J.H. et al. Mitochondrial network complexity and pathological decrease in complex I activity are tightly correlated in isolated human complex I deficiency. *Am. J. Physiol. Cell Physiol.* **289**, C881–C890 (2005).
- Koopman, W.J.H., Visch, H.J., Smeitink, J.A.M. & Willems, P.H.G.M. Simultaneous, quantitative measurement and automated analysis of mitochondrial morphology, mass, potential and motility in living human skin fibroblasts. *Cytometry A* **69A**, 1–12 (2006).
- Distelmaier, F. et al. Life cell quantification of mitochondrial membrane potential at the single organelle level. *Cytometry A* **73**, 129–138 (2008).
- Willems, P.H.G.M., Smeitink, J.A.M. & Koopman, W.J.H. Mitochondrial dynamics in human NADH:oxidoreductase deficiency. *Int. J. Biochem. Cell Biol.* **41**, 1773–1783 (2009).
- Nooteboom, M., Forkink, M., Willems, P.H.G.M. & Koopman, W.J.H. Live-cell quantification of mitochondrial functional parameters. in *Neuromethods 70: Visualization Techniques, from Immunohistochemistry to Magnetic Resonance Imaging* (ed. Badoer, E.) Chapter 6 (Springer, New York, 2012).
- Blanchet, L., Buydens, L.M.C., Smeitink, J.A.M., Willems, P.H.G.M. & Koopman, W.J.H. Isolated mitochondrial complex I deficiency: explorative pattern analysis of patient cell parameters. *Curr. Pharm. Des.* **17**, 4023–4033 (2011).
- Blanchet, L. et al. Analysis of small molecule phenotypic effects using combined mitochondrial morpho-functional fingerprinting and machine learning. *Sci. Rep.* **5**, 8035 (2015).
- Koopman, W.J.H. et al. Human NADH: oxidoreductase deficiency: radical changes in mitochondrial morphology? *Am. J. Physiol. Cell Physiol.* **293**, C22–C29 (2007).
- Koopman, W.J.H. et al. Inherited complex I deficiency is associated with faster protein diffusion in the matrix of moving mitochondria. *Am. J. Physiol. Cell Physiol.* **294**, C1124–C1132 (2008).
- Lansing-Taylor, D. Past, present and future of high content screening and the field of cellomics. in *High Content Screening: A Powerful Approach to Systems Cell Biology and Drug Discovery* (eds. Lansing-Taylor, D., Haskins, J.R. & Giuliano, K.A.) (Humana Press, Totowa, NJ, USA, 2007).
- Feng, Y., Mitchison, T.J., Bender, A., Young, D.W. & Tallarico, J.A. Multi-parameter phenotypic profiling: using cellular effects to characterize small-molecule compounds. *Nat. Rev. Drug Discov.* **8**, 567–578 (2009).
- Zanella, F., Lorens, J.B. & Link, W. High content screening: seeing is believing. *Trends Biotechnol.* **28**, 237–245 (2010).
- Bast, A. & Haenen, G.R.M.M. Ten misconceptions about antioxidants. *Trends Pharmacol. Sci.* **34**, 430–436 (2013).
- Wiemerslage, L. & Lee, D. Quantification of mitochondrial morphology in neurites of dopaminergic neurons using multiple parameters. *J. Neurosci. Methods* **262**, 56–65 (2016).
- Sommer, C. & Gehrlich, D.W. Machine learning in cell biology – teaching computers to recognize phenotypes. *J. Cell Sci.* **126**, 5529–5539 (2013).
- Peng, J.Y. et al. Automatic morphological subtyping reveals new roles of caspases in mitochondrial dynamics. *PLoS Comput. Biol.* **7**, e1002212 (2011).
- Reis, Y. et al. Multi-parametric analysis and modeling of relationships between mitochondrial morphology and apoptosis. *PLoS One* **7**, e28694 (2012).
- Ahmad, T. et al. Computational classification of mitochondrial shapes reflects stress and redox state. *Cell Death Dis.* **4**, e461 (2013).
- Leonard, A.P. et al. Quantitative analysis of mitochondrial morphology and membrane potential in living cells using high-content imaging, machine learning, and morphological binning. *Biochim. Biophys. Acta* **1853**, 348–360 (2015).
- Nikolaisen, J. et al. Automated quantification and integrative analysis of 2D and 3D mitochondrial shape and network properties. *PLoS One* **9**, e101365 (2014).
- Farrand, L. et al. An improved quantitative approach for the assessment of mitochondrial fragmentation in chemoresistant ovarian cancer cells. *PLoS One* **8**, e74008 (2014).
- Rizk, A. et al. Segmentation and quantification of subcellular structures in fluorescence microscopy images using Squash. *Nat. Protoc.* **9**, 586–596 (2014).
- Lautenschläger, J. et al. Novel computer vision algorithm for the reliable analysis of organelle morphology in whole cell 3D images - A pilot study for the quantitative evaluation of mitochondrial fragmentation in amyotrophic lateral sclerosis. *Mitochondrion* **25**, 49–59 (2015).

PROTOCOL

44. Lihavainen, E., Kislin, M., Toptunov, D., Khiroug, L. & Ribeiro, A.S. Automatic quantification of mitochondrial fragmentation from two-photon microscope images of mouse brain tissue. *J. Microsc.* **260**, 338–351 (2015).
45. Hugelier, S. *et al.* Sparse deconvolution of high-density super-resolution images. *Sci. Rep.* **6**, 21413 (2016).
46. McClatchey, P.M., Keller, A.C., Bouchard, R., Knaub, L.A. & Reusch, J.E.B. Fully automated software for quantitative measurements of mitochondrial morphology. *Mitochondrion* **26**, 58–71 (2016).
47. Giuly, R.J., Martone, M.E. & Ellisman, M.H. Method: automatic segmentation of mitochondria utilizing patch classification, contour pair classification, and automatically seeded level sets. *BMC Bioinformatics* **13**, 29 (2012).
48. Lihavainen, E., Makela, J., Spelbrink, J.N. & Ribeiro, A.S. Mitoe: automatic analysis of mitochondrial dynamics. *Bioinformatics* **28**, 1050–1051 (2012).
49. Mumcuoglu, E.U. *et al.* Computerized detection and segmentation of mitochondria on electron microscope images. *J. Microsc.* **246**, 248–265 (2012).
50. Dietlmaier, J., Ghita, O., Duessmann, H., Prehn, J.H. & Whelan, P.F. Unsupervised mitochondria segmentation using recursive spectral clustering and adaptive similarity models. *J. Struct. Biol.* **184**, 401–408 (2013).
51. Bros, H., Hauser, A., Niesner, R. & Infante-Duarte, C. Assessing mitochondrial movement within neurons: manual versus automated tracking methods. *Traffic* **16**, 906–917 (2015).
52. Kandel, J., Chou, P. & Eckmann, D.M. Automated detection of whole-cell mitochondrial motility and its dependence on cytoarchitectural integrity. *Biotechnol. Bioeng.* **112**, 1395–1405 (2015).
53. Tasel, S.F., Mumcuoglu, E.U., Hassanpour, R.Z. & Perkins, G. A validated active contour method driven by parabolic arc model for detection and segmentation of mitochondria. *J. Struct. Biol.* **194**, 253–271 (2016).
54. Forkink, M. *et al.* Mitochondrial hyperpolarization during chronic complex I inhibition is sustained by low activity of complex II, III, IV and V. *Biochim. Biophys. Acta* **1837**, 1247–1256 (2014).
55. Nicholls, D.G. Simultaneous monitoring of ionophore- and inhibitor-mediated plasma and mitochondrial membrane potential changes in cultured neurons. *J. Biol. Chem.* **281**, 14864–14874 (2006).
56. Hüser, J., Rechenmacher, C.E. & Blatter, L.A. Imaging the permeability transition in single mitochondria. *Biophys. J.* **74**, 2129–2137 (1998).
57. Falchi, A.M., Isola, R., Diana, A., Putzolu, M. & Diaz, G. Characterization of depolarization and repolarization phases of mitochondrial membrane potential fluctuations induced by tetramethylrhodamine methyl ester photoactivation. *FEBS J.* **272**, 1649–1659 (2005).
58. Blanchet, L., Grefte, S., Smeitink, J.A.M., Willems, P.H.G.M. & Koopman, W.J.H. Photo-induction and automated quantification of reversible mitochondrial permeability transition pore opening in primary mouse myotubes. *PLoS One* **9**, e114090 (2014).
59. Wang, X.M. *et al.* A new microcellular cytotoxicity test based upon calcein AM release. *Hum. Immunol.* **37**, 264–270 (1993).
60. Homolya, L. *et al.* Fluorescent cellular indicators are extruded by the multidrug resistance protein. *J. Biol. Chem.* **268**, 21496–21496 (1993).
61. Sternberg, S.R. Biomedical image processing. *Computer* **16**, 22–34 (1983).
62. Russ, J.C. & Neal, F.B. *The Image Processing Handbook* 7th edn. (CRC press, Boca Raton, FL, 2016).
63. Bray, M.A. & Carpenter, A. Advanced assay development guidelines for image-based high content screening and analysis. in *Assay Guidance Manual* (eds. Sittampalam, G.S. *et al.*) (Eli Lilly & Company and the National Center for Advancing Translational Sciences, Bethesda, MD, 2004).
64. Tigges, J. *et al.* The hallmarks of fibroblast aging. *Mech. Ageing Dev.* **138**, 26–44 (2014).
65. Massart, D.L. *et al.* *Handbook of Chemometrics and Qualimetrics* (Amsterdam, the Netherlands: Elsevier, 1997).
66. Tukey, J.W. *Exploratory Data Analysis* 1st edn. (Addison-Wesley, Boston, MA, 1977).
67. Ringnér, M. What is principal component analysis? *Nat. Biotechol.* **26**, 303–304 (2008).
68. Bro, R. & Smilde, A.K. Principal component analysis. *Anal. Methods* **6**, 2812–2831 (2014).
69. Brown, J.D. Choosing the right number of components of factors in PCA and EFA. *Shiken: JALT testing & evaluation SIG Newsletter* **13**(2), 19–23 (2009).
70. Lemasters, J.J. & Ramshesh, V.K. Imaging of mitochondrial polarization and depolarization with cationic fluorophores. *Methods Cell. Biol.* **80**, 283–295 (2007).
71. Elceirí, K.W. *et al.* Biological imaging software tools. *Nat. Methods* **9**, 697–710 (2012).
72. Kitami, T. *et al.* A chemical screen probing the relationship between mitochondrial content and cell size. *PLoS One* **7**, e33755 (2012).
73. Gonzalez, R.C. & Woods, R.E. *Digital Image Processing* 3rd edn. (Pearson Prentice Hall, Upper Saddle River, NJ, 2008).

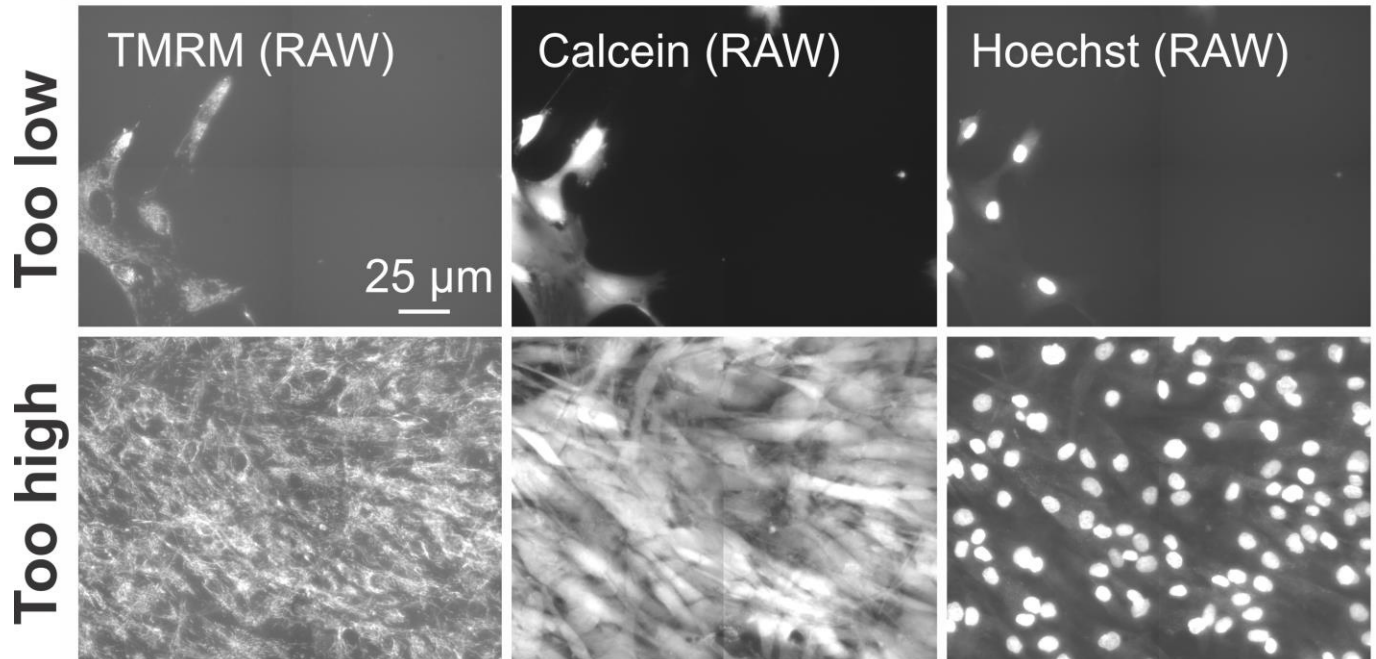


Supplementary Figure 1

Importance of the threshold (T) gray value for correct calculation of the BIN and MSK images.

(A) Typical RAW calcein image (left image) and the effect of various thresholds (numerals depict the threshold gray value) on the resulting binary (BIN) image. (B) Same as panel A but now for the RAW TMRM image of the same cells. (C) TMRM MSK image calculated using the BIN images in panel B. (D) Average value of *Casum* (total area of the objects in the calcein BIN image) and *Asum* (total area of the mitochondrial objects in the TMRM MSK image) for various threshold values. (E) Average value of *AR* (aspect ratio of mitochondrial objects), *F* (form factor: length and degree of branching of mitochondrial objects) and *Mm* (mitochondrial mass) in the TMRM MSK image for various threshold values. (F) Average value of *Dm* (mitochondrial TMRM

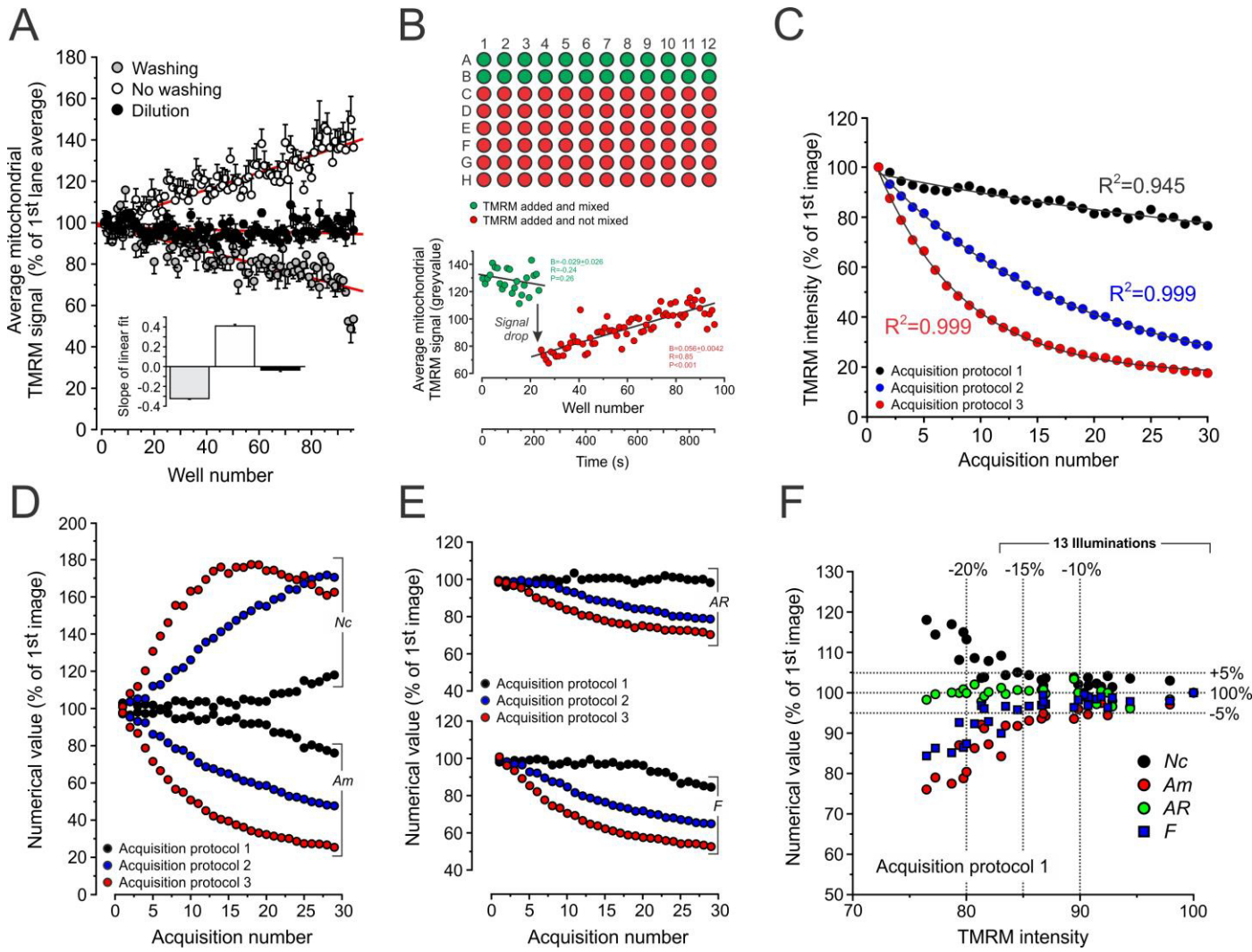
intensity in TMRM MSK image), Ot (the total number of mitochondrial objects in the TMRM MSK image), Am (the area of individual mitochondrial objects in the TMRM MSK image) and Nc (the number of mitochondria per cell; calculated by combining information from the TMRM MSK and Hoechst BIN image) for various threshold values. Using a threshold value of 40 yielded the correct values of key descriptors between 3-6 (F), 2-3 (AR) and 50-150 (Nc), compatible with previous manual analysis (*e.g.* Koopman et al., 2005a; Koopman et al., 2005b; Koopman et al., 2006; Koopman et al., 2008a; Distelmaier et al., 2008; Distelmaier et al., 2012; Distelmaier et al., 2015).



Supplementary Figure 2

Illustration of too low and too high cell density.

Since images are automatically acquired for each well there is no user-control regarding which cells are imaged. Although this strategy avoids user-induced bias, it requires that the average number of imaged cells is similar between individual wells. The latter is also important to allow standardized image processing, statistical analysis and QC. This figure provides typical examples of too low and too high cell densities (relative to the proper density depicted in **Figure 5**). The protocol described in the main text was used to acquire the images in this figure.

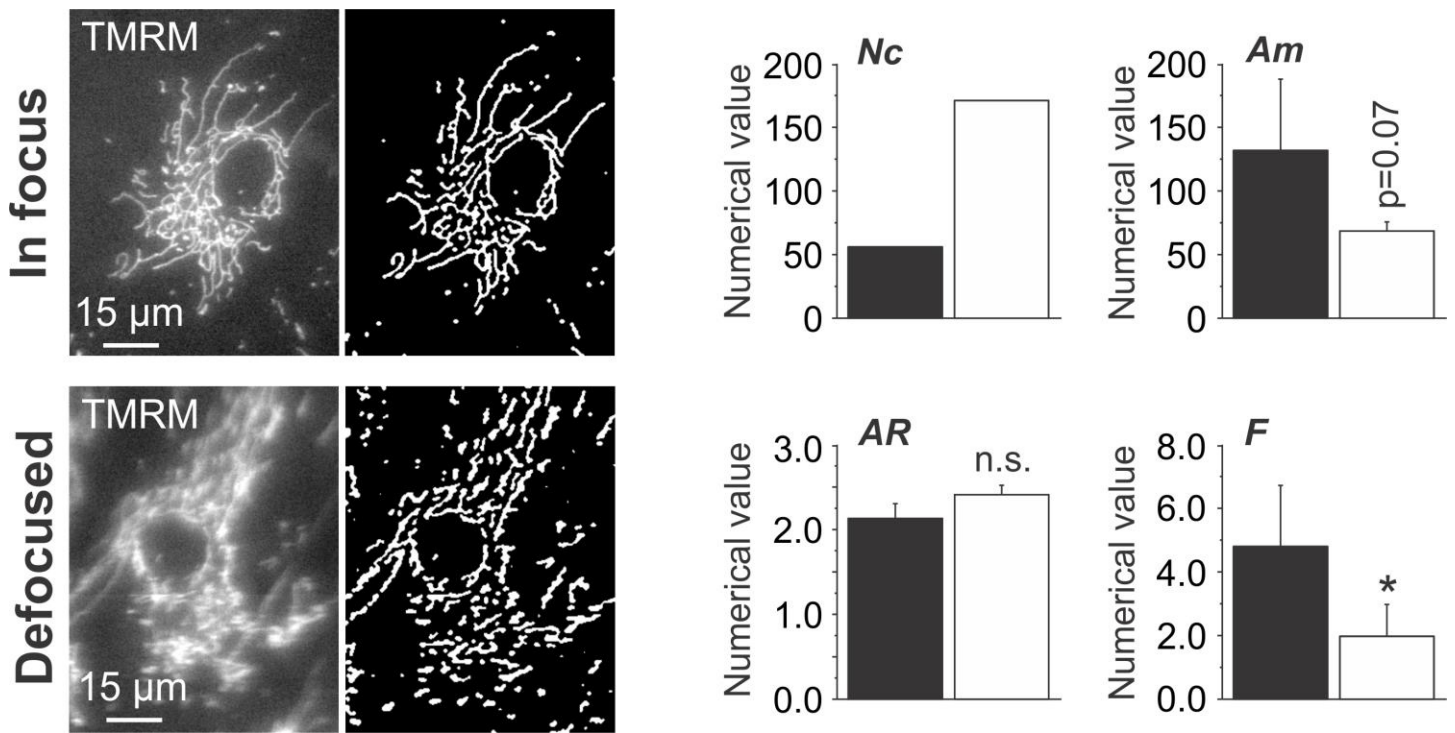


Supplementary Figure 3

Importance of the presence of extracellular TMRM, well mixing and illumination intensity for TMRM descriptor analysis.

This figure illustrates why it is important to have TMRM present outside the cell during image TMRM acquisition, why wells need to be properly mixed following TMRM addition, and the artefact-inducing effect of too high illumination intensities. Unless stated otherwise, the experimental data in this figure was acquired using the experimental protocol described in the main text. **(A)** Importance of the presence of extracellular TMRM during TMRM image acquisition. In this experiment the calcein/Hoechst loading and imaging steps were omitted. Three different manoeuvres were tested (using 5 plates/days for each condition), thereby modifying step 15 of the protocol as follows: “Washing” condition (gray symbols; two washing steps were performed using 100 μ l assay medium; 100 μ l of assay medium was present in each well during image acquisition); “No washing” condition (open symbols; nothing was done to the plate after step 13); “Dilution” condition (black symbols; 100 μ l assay medium was added to each well without washing and mixing). Only for the last condition, the fluorescence signal remained stable as indicated by the slope (inset) of a linear fit (red line). All data were normalized to the average of the first row (row A) of the plate. **Fitting results:** P<0.001,

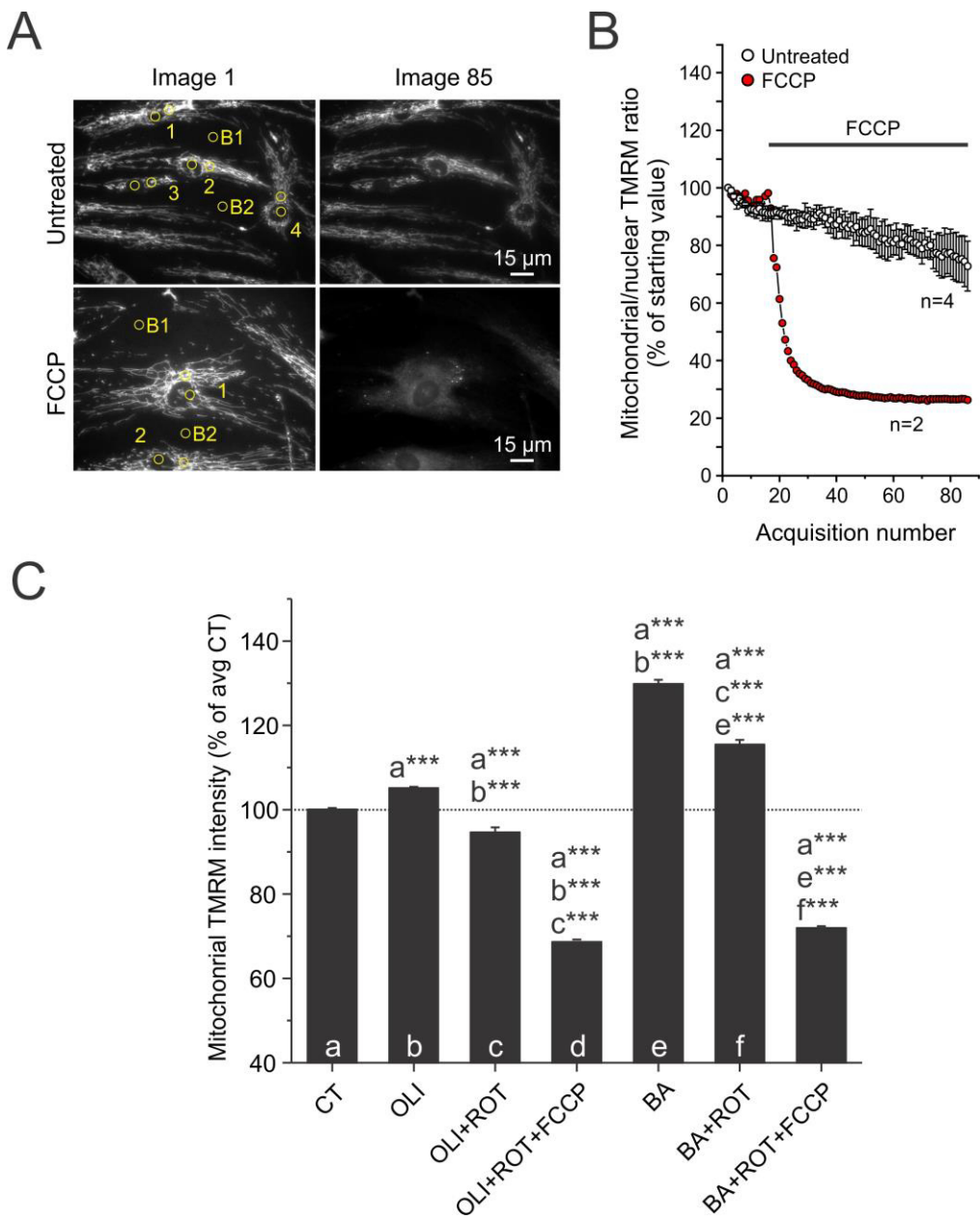
$R=-0.83$ (Washing condition); $P<0.001$, $R=0.91$ (No washing condition); $P=0.029$, $R=-0.22$ (Dilution condition). **(B)** Importance of mixing after TMRM addition to the well. The following steps of the protocol were modified: Step 13 (TMRM was added and mixed by pipetting up and down 4 times, but only in row A and B. For row C to H, TMRM was added but not mixed. Calcein/Hoechst staining and imaging were not required here. Only in the mixed wells (green), the TMRM signal was stable (*i.e.* the fitted line had no significant slope). **(C)** Effect of TMRM illumination intensity on the TMRM fluorescence signal. In this experiment, 30 subsequent images of the same well were acquired at the same position (Option in BD AttoVision Software: image acquisition option/acquire button/30 data points. Three different acquisition protocols were used with the following settings: Protocol 1 (Exposure time: 0.1 s; Excitation B: 548/20; Excitation dichroic: 40%; Lamp B intensity: 60%), protocol 2 (Exposure time: 0.1 s; Excitation B: 548/20; Excitation dichroic: open; Lamp B intensity: 80%), protocol 3 (Exposure time: 0.1 s; Excitation B: 548/20; Excitation dichroic: open; Lamp B intensity: 100%). Acquisition protocol 1 (used in the protocol) displayed the lowest drop in TMRM signal. **Fitting results:** TMRM intensity curves were fitted using a mono-exponential equation ($y=y_0+A_1e^{-t/\tau}$, with τ being the decay time constant). The fitted τ values equalled: 44.0 ± 23.4 (acquisition protocol 1), 17.4 ± 0.384 (acquisition protocol 2) and 7.56 ± 0.129 (acquisition protocol 3). **(D)** Effect of the three illumination protocols on the calculated mitochondrial area (Am) and number of mitochondrial objects per cell (Nc). The more the TMRM signal drops, the greater the erroneous apparent increase in Am and Nc . **(E)** Similar to panel D but now for the calculated mitochondrial aspect ratio (AR) and form factor (F). **(F)** Values of calculated key mitochondrial descriptors (Nc , Am , AR and F ; y-axis) as a function of TMRM intensity (x-axis) for acquisition protocol 1. About 13 illuminations can be carried out (*i.e.* 13 images can be acquired) before the (10-15%) drop in TMRM intensity affects descriptor quantification.



Supplementary Figure 4

Illustration of the effect of image defocusing on TMRM-reported mitochondrial morphology descriptors.

It is of the greatest importance that the acquired images are optimally focused, since defocusing will affect the extracted numerical data in a descriptor-dependent manner. This figure illustrates the effects of image defocusing on key mitochondrial descriptors. Typically, defocused images contain “artificial” small non-mitochondrial objects after image processing. The latter results in an apparent increase in the number of mitochondrial objects per cell (*Nc*), and a decrease in mitochondrial size (*Am*) and form factor (*F*). **Statistics:** Significant differences between the focused and defocused condition were assessed using an unpaired independent Student’s test and presented by: * ($P < 0.05$), the actual P -value (*Am*) and by non-significant (n.s.). The protocol described in the main text was used to acquire the images in this figure.

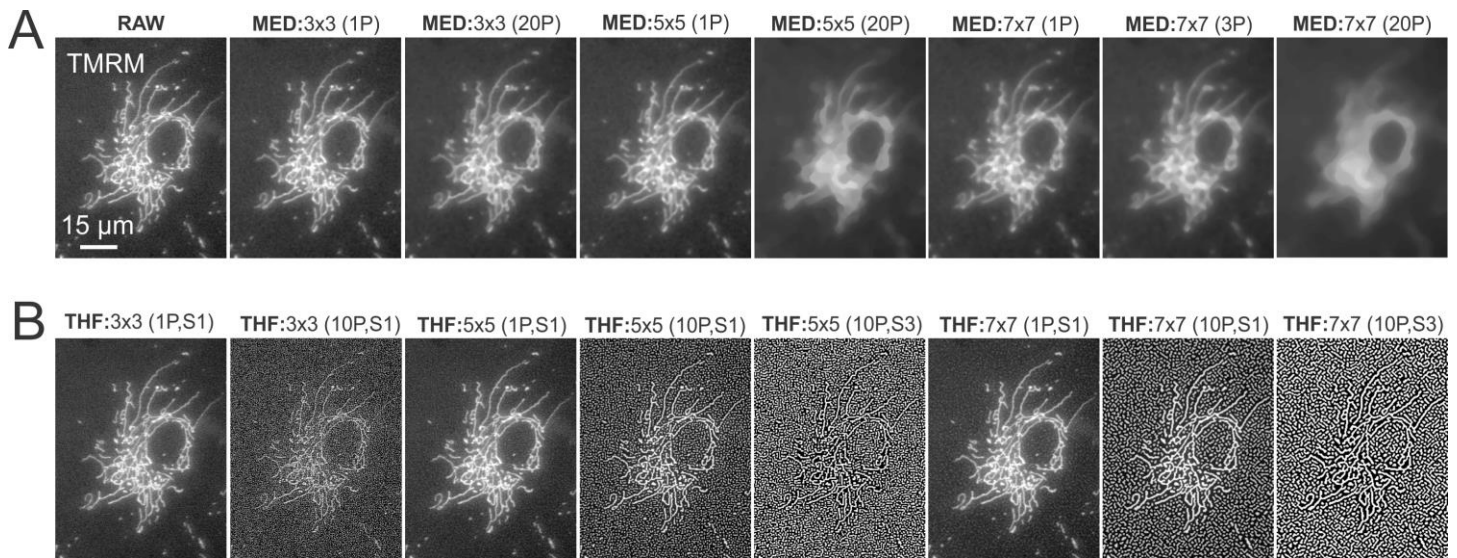


Supplementary Figure 5

Control for TMRM autoquenching, detectability of $\Delta\psi$ hyperpolarization and effect of the mitochondrial uncoupler FCCP.

This figure illustrates how to check if the TMRM fluorescence signal is affected by autoquenching and whether $\Delta\psi$ depolarization and hyperpolarization can be detected by decreased and increased mitochondrial TMRM accumulation, respectively. **(A)** Eighty-five consecutive TMRM images were acquired from the same well. The displayed typical image-pairs illustrate the effect of the mitochondrial uncoupler p-trifluoromethoxy carbonyl cyanide phenyl hydrazine (FCCP, 10 μ M; #370-86-5; Sigma-Aldrich, St. Louis, MO, USA) on mitochondrial TMRM staining (upper vs. lower panel). Numerals mark individual cells and regions of interest (ROIs; yellow) mark the nuclear and mitochondrial compartment (yellow circles). **(B)** Average ratio between TMRM intensity

in the mitochondrial and nuclear compartments calculated using the ROIs in panel A for untreated (n=4 cells) and FCCP-treated (n=2) cells. Repeated illumination induces a gradual drop in ratio (photobleaching) in the untreated cells. FCCP induces a smooth drop in the ratio signal, indicating the absence of TMRM autoquenching. If the latter would be the case, FCCP would first induce an increase in the signal (due to TMRM dequenching in the mitochondrial matrix), followed by a decrease. **(C)** Effect of subsequent acute addition of the F_oF₁-ATPase inhibitor Oligomycin A (OLI; 1 μM; #1404-19-9; Sigma-Aldrich), the mitochondrial complex I inhibitor Rotenone (ROT; 1 μM; #83-79-4; Sigma-Aldrich) and FCCP (10 μM) on mitochondrial TMRM fluorescence intensity. In a second type of experiment, Bonkrekic acid (BA; 50 μM; #11076-19-0; Sigma-Aldrich) was acutely added to inhibit the electrogenic mitochondrial ATP/ADP translocator (ANT). This was followed by subsequent addition of ROT and FCCP. **Statistics:** Significant differences with the indicated columns (a,b,c,d,e,f) was assessed using an unpaired independent Student's test (Origin Pro 6.1) and presented by: *** (P<0.001). **Experimental details:** Options used in the BD attovision software: “*Montage Capture Setup*”, “*INACTIVE MONTAGE*”, “*1 Frame*”. MACRO on BD attovision software: Experiment 1 (30 (CT) TMRM image acquisitions of the same well; 30 s pause during which 1 μM Oligomycin (OLI) is added by pipetting; 30 TMRM image acquisitions of the same well; 30 s pause during which 1 μM Rotenone (ROT) is added; 30 TMRM image acquisitions of the same well; 30 s pause during which 10 μM FCCP is added; 30 TMRM image acquisitions of the same well); Experiment 2 (30 (CT) TMRM image acquisitions of the same well; 30 s pause during which 50 μM Bongkrekic acid (BA) is added; 30 TMRM image acquisitions of the same well; 30 s pause during which 1 μM Rotenone (ROT) is added; 30 TMRM image acquisitions of the same well; 30 s pause during with 10 μM FCCP is added; 30 TMRM image acquisitions of the same well). **Remarks:** Care should be taken that during addition of the inhibitors the pipette tip does not touch the plate to avoid altering the field of view. Inhibitors are added at twice their final concentration in a (relatively large) volume of 100 μl to each well (which contains 100 μl of fluid). This ensures complete and rapid mixing.



Supplementary Figure 6

Visualization of the effect of median (MED) and top-hat (THF) spatial filtering on the TMRM image.

Proper use of the MED and THF filters to reduce noise and isolate mitochondrial objects, respectively, is crucial for proper subsequent calculation of the binary image (BIN). The latter image represents white mitochondrial objects on a black background (for the complete processing pipeline see **Fig. 5C**). In this protocol, we have established the correct size of the MED and THF filter, how often they should be applied (“passes”) and, in case of the THF filter, its strength (“S”). For details about these parameters see the information in **Box 1** provided in the main text. **(A)** Effect of various MED filter settings on the TMRM image (RAW). **(B)** Effect of various THF filter settings on the TMRM image (RAW).

Supplementary Table 1 | Use of the quantification protocol in various cell types

Cell type	Staining	Imaging	Descriptors	Reference
BGM	mtEYFP	V-CLSM	<i>Am, AR, F, Nc, Mm</i>	Tronstad et al., 2014
CE	mtGFP	CLSM	<i>AR, F</i>	Hoffmann et al., 2009
CV1-4A	mtDsRed1	EPIF	<i>Am, AR, Nc</i>	De Vos et al., 2005
CHO	R123	EPIF	<i>F, Nc</i>	Distelmaier et al., 2012
Clone 9	mtRFP/mtGFP	EPIF	<i>AR, F</i>	Hom et al., 2007
COS-7	MTDR/mtGFP	EPIF	<i>AR, F</i>	Buhlman et al., 2014
CPA	TMRM	CLSM	<i>Am, AR, F, Fi</i>	Matthews et al., 2010
CPH	TMRM	CLSM	<i>Am, AR, F, Fi</i>	Matthews et al., 2010
H9c2	mtRFP	EPIF	<i>AR, F</i>	Yu et al., 2006
H9c2	MTR	EPIF	<i>AR, F</i>	Yu et al., 2008
HEK293	MTR	V-CLSM	<i>F, Nc</i>	Vogel et al., 2007
HeLa	R123	V-CLSM	<i>F, Nc</i>	Distelmaier et al., 2012
HPM	R123	V-CLSM	<i>AR, F, Nc</i>	Eisenberg et al., 2008
HUVECs	MTG	EPIF	<i>AR, F</i>	Lugus et al., 2011
HUVECs	mtGFP	CLSM	<i>Am, F, Nc, Pm</i>	Nikolaisen et al., 2014
M17HN	mtDsRed2	CLSM	<i>AR</i>	Wang et al., 2012b
MEFs	TMRM	EPIF	<i>F, Nc, Fi</i>	Distelmaier et al., 2012
MEFs	TMRM	EPIF	<i>Am, F, Mm, Nc</i>	Heeman et al., 2011
MM	Mt-roGFP2	EPIF	<i>F</i>	Cunniff et al., 2013
MPM	MTR	V-CLSM	<i>Am, AR, F, Nc, Mm</i>	Tronstad et al., 2014
N2a	R123	V-CLSM	<i>AR, F, Nc</i>	Coussee et al., 2011
PHSF	R123	V-CLSM	<i>AR, F, Fi, Nc, F/Nc</i>	Koopman et al., 2005a
PHSF	R123	V-CLSM	<i>AR, F, Nc</i>	Koopman et al., 2005b
PHSF	R123	V-CLSM	13 different	Koopman et al., 2006
PHSF	TMRM	EPIF	<i>Am, F, Fi, Nc</i>	Komen et al., 2007
PHSF	mtEYFP	V-CLSM	<i>F, Nc</i>	Koopman et al., 2007b
PHSF	mtGFP/TMRM	EPIF	<i>Fi</i>	Distelmaier et al., 2008
PHSF	TMRM	EPIF	<i>Fi</i>	Hoefs et al., 2008
PHSF	mtGFP/TMRM	EPIF	<i>Am, AR, F, Fi, Lm, Mm, Nc, Wm</i>	Koopman et al., 2008a
PHSF	R123	V-CLSM	<i>AR, F, Nc</i>	Mortiboys et al., 2008
PHSF	TMRM	EPIF	<i>Fi</i>	Distelmaier et al., 2009
PHSF	R123	V-CLSM	<i>F, Nc</i>	Willemse et al., 2009
PHSF	MTG	EPIF	<i>AR, F</i>	Burbulla et al., 2010
PHSF	TMRM	EPIF	<i>AR, F, Fi, Nc</i>	Jonckheere et al., 2011
PHSF	TMRM	EPIF	<i>Am, F</i>	Baracca et al., 2013
PHSF	MTG	EPIF	<i>Am, AR, F</i>	Grau et al., 2013
PHSF	TMRM	EPIF	<i>F, Nc</i>	Szklarczyk et al., 2013
PHSF	TMRM	EPIF	<i>Am, AR, F, Fi, Mm, Nc</i>	Szklarczyk et al., 2013
PHSF	TMRM	EPIF	<i>Am, AR, F, Nc</i>	Willemse et al., 2013
PHSF	TMRM/CM-H ₂ DCF	EPIF	<i>Am, AR, F, Nc, Ac</i>	Distelmaier et al., 2015
PHSF	TMRM	EPIF	31 different	Blanchet et al., 2015
PMMF	R123	V-CLSM	<i>Am, F, Nc</i>	Valsecchi et al., 2013
PMSF	R123	V-CLSM	<i>Am, F, Nc</i>	Valsecchi et al., 2013
RPAC	R123	V-CLSM	<i>Am, AR, F, Nc, Mm</i>	Tronstad et al., 2014
SH-SY5Y	mtDsRed1	EPIF	<i>AR, F</i>	Burbulla et al., 2010
SH-SY5Y	MtDsRed2	CLSM	<i>AR</i>	Wang et al., 2011
SH-SY5Y	MtDsRed2	CLSM	<i>AR</i>	Wang et al., 2012a

Abbreviations: *Ac*, area of cell; *Am*, area of mitochondrial object; *AR*, aspect ratio of mitochondrial object; BGM, Buffalo Green Monkey kidney cells; CE, intact *C. elegans*; CHO, Chinese Hamster Ovary cells; Clone9, Rat liver cells; CLSM, Confocal Laser Scanning Microscopy; CM-H₂DCF, 5-(and-6)-chloromethyl-2',7'-dichlorodihydrofluorescein; COS-7, African green monkey kidney cells; CPA, Chicken Primary Astrocytes; CPH, Chicken Primary Hepatocytes; EPIF, epifluorescence microscopy; *F*, formfactor of mitochondrial object; *Fi*, fluorescence intensity of mitochondrial object; H9c2, Rat heart myoblasts; HEK293, Human Embryonic Kidney cells; HeLa, Human epitheloid cervix carcinoma; HPM, Human Primary Myoblasts; HUVECs, Human Umbilical Vein Endothelial Cells; *Lm*, length of mitochondrial object; M17HN, M17 Human Neuroblastoma; MEFs, Mouse Embryonic Fibroblasts; *Mm*, mitochondrial mass; MM, Malignant Mesothelioma cells; MPM, Mouse Primary Myoblasts; MTDR, Mitotracker Deep Red; mtEYFP, mitochondria-targeted Enhanced Yellow Fluorescent Protein; MTG, Mitotracker Green; mtGFP, mitochondria-targeted Green Fluorescent Protein; MTR, Mitotracker Red CMXRos; MtRFP, mitochondria-targeted Red Fluorescent Protein; Mt-roGFP2, mitochondria-targeted redox-sensitive GFP2; N2a, Mouse Neuroblastoma cells; *Nc*, number of mitochondrial objects per cell; PHSF, Primary Human Skin Fibroblasts; *Pm*, perimeter of mitochondrial object; PMMF, Primary Mouse Muscle-derived Fibroblasts; PMSF, Primary Mouse Skin-derived Fibroblasts; R123, rhodamine 123; RPAC, Rat Primary Pancreatic Acinar Cells; SH-SY5Y, Human neuroblastoma cells; TMRM, tetramethyl rhodamine methyl ester; V-CLSM, Videorate Confocal Laser Scanning Microscopy; *Wm*, width of mitochondrial object. This table was adapted from: [Tronstad et al., 2014](#).

Supplementary Table 2 | Composition of the used media

CULTURE MEDIUM		ASSAY MEDIUM	
Components	mM	Components	mM
Amino Acids		Amino Acids	
Glycine	0.66667	Glycine	0.66667
L-Alanine	0.28090	L-Alanine	0.28090
L-Arginine hydrochloride	0.33175	L-Arginine hydrochloride	0.33175
L-Aspartic acid	0.22556	L-Aspartic acid	0.22556
L-Cysteine hydrochloride-H ₂ O	0.00057	L-Cysteine hydrochloride-H ₂ O	0.00057
L-Cystine 2HCl	0.10833	L-Cystine 2HCl	0.10833
L-Glutamic Acid	0.51020	L-Glutamic Acid	0.51020
L-Glutamine	0.68493	L-Glutamine	0.68493
L-Histidine hydrochloride-H ₂ O	0.10419	L-Histidine hydrochloride-H ₂ O	0.10419
L-Hydroxyproline	0.07634	L-Hydroxyproline	0.07634
L-Isoleucine	0.30534	L-Isoleucine	0.30534
L-Leucine	0.45802	L-Leucine	0.45802
L-Lysine hydrochloride	0.38251	L-Lysine hydrochloride	0.38251
L-Methionine	0.10067	L-Methionine	0.10067
L-Phenylalanine	0.15152	L-Phenylalanine	0.15152
L-Proline	0.34783	L-Proline	0.34783
L-Serine	0.23810	L-Serine	0.23810
L-Threonine	0.25210	L-Threonine	0.25210
L-Tryptophan	0.04902	L-Tryptophan	0.04902
L-Tyrosine disodium salt dihydrate	0.22222	L-Tyrosine disodium salt dihydrate	0.22222
L-Valine	0.21368	L-Valine	0.21368
Vitamins		Vitamins	
Alpha-tocopherol Phosphate	0.00001	Alpha-tocopherol Phosphate	0.00001
Ascorbic Acid	0.00028	Ascorbic Acid	0.00028
Biotin	0.00004	Biotin	0.00004
Choline chloride	0.00357	Choline chloride	0.00357
D-Calcium pantothenate	0.00002	D-Calcium pantothenate	0.00002
Folic Acid	0.00002	Folic Acid	0.00002
Menadione (Vitamin K3)	0.00006	Menadione (Vitamin K3)	0.00006
Niacinamide	0.00020	Niacinamide	0.00020
Nicotinic acid (Niacin)	0.00020	Nicotinic acid (Niacin)	0.00020
Para-Aminobenzoic Acid	0.00036	Para-Aminobenzoic Acid	0.00036
Pyridoxal hydrochloride	0.00012	Pyridoxal hydrochloride	0.00012
Pyridoxine hydrochloride	0.00012	Pyridoxine hydrochloride	0.00012
Riboflavin	0.00003	Riboflavin	0.00003
Thiamine hydrochloride	0.00003	Thiamine hydrochloride	0.00003
Vitamin A (acetate)	0.00030	Vitamin A (acetate)	0.00030

Vitamin D2 (Calciferol)	0.00025	Vitamin D2 (Calciferol)	0.00025
i-Inositol	0.00028	i-Inositol	0.00028
Inorganic Salts		Inorganic Salts	
Calcium Chloride (CaCl ₂) (anhyd.)	1.80180	Calcium Chloride (CaCl ₂) (anhyd.)	1.80180
Ferric nitrate (Fe(NO ₃) ₃ ·9H ₂ O)	0.00173	Ferric nitrate (Fe(NO ₃) ₃ ·9H ₂ O)	0.00173
Magnesium Sulfate (MgSO ₄) (anhyd.)	0.81392	Magnesium Sulfate (MgSO ₄) (anhyd.)	0.81392
Potassium Chloride (KCl)	5.33333	Potassium Chloride (KCl)	5.33333
Sodium Bicarbonate (NaHCO ₃)	26.1904	Sodium Bicarbonate (NaHCO ₃)	26.1904
Sodium Chloride (NaCl)	105.172	Sodium Chloride (NaCl)	117.241
Sodium Phosphate monobasic (NaH ₂ PO ₄)	1.01449	Sodium Phosphate monobasic (NaH ₂ PO ₄)	1.01449
Other Components		Other Components	
2-deoxy-D-ribose	0.00373	2-deoxy-D-ribose	0.00373
Adenine sulfate	0.02475	Adenine sulfate	0.02475
Adenosine 5'-phosphate	0.00058	Adenosine 5'-phosphate	0.00058
Adenosine 5'-triphosphate	0.00165	Adenosine 5'-triphosphate	0.00165
Cholesterol	0.00052	Cholesterol	0.00052
D-Glucose (Dextrose)	5.55556	D-Glucose (Dextrose)	5.55556
Glutathione (reduced)	0.00016	Glutathione (reduced)	0.00016
Guanine hydrochloride	0.00160	Guanine hydrochloride	0.00160
HEPES	25.0420	HEPES (add yourself)	25.0420
Hypoxanthine Na	0.00294	Hypoxanthine Na	0.00294
Phenol Red	0.05313	Phenol Red	0.0
Ribose	0.00333	Ribose	0.00333
Sodium Acetate	0.60976	Sodium Acetate	0.60976
Thymine	0.00238	Thymine	0.00238
Tween 80®	Infinity	Tween 80®	Infinity
Uracil	0.00268	Uracil	0.00268
Xanthine-Na	0.00224	Xanthine-Na	0.00224

Culture medium: Cells were cultured in culture medium (Medium 199, HEPES; #12340-030, Invitrogen, Breda, The Netherlands). To the culture medium was added: 10% (v/v) fetal calf serum (FBS; #758093, Greiner Bio-One, GmbH, Germany), 100 IU/ml penicillin and 100 IU/ml streptomycin (#30-002-CI, Corning, NY, USA).

Assay medium: TMRM, Calcein-AM and Hoechst 33258 were diluted in assay medium (Medium 199, no phenol red; #11043-023; Invitrogen, Breda, The Netherlands). To the assay medium was added: 25 mM HEPES (HEPES (1M); #15630-08, Invitrogen, Breda, The Netherlands). Washing steps were done with the assay medium; images were acquired in the assay medium.

Supplementary Table 3 | Detailed BD Pathway® 855 settings

96 WELL PLATE GREINER 655090 CELLSTAR® 96W Microplate

Setting	Calcein	Hoechst 33258	TMRM
Geometry setup			
Objective	40x Olympus	40x Olympus	40x Olympus
Ring value	0.17	0.17	0.17
Binning	1x1=0.156617µm/pixel	1x1=0.156617µm/pixel	1x1=0.156617µm/pixel
Light path			
Lamp A Transmittance	100%	100%	n.a.
Lamp B Transmittance	n.a.	n.a.	60%
Excitation A	488/10	380/10	n.a.
Excitation B	n.a.	n.a.	548/20
Excitation Dichroic	OPEN	OPEN	40%B
Emission	FURA/FITC	400DCLP	FURA/TRITC
Epifluorescence dichroic	515LP	435LP	FURA/TRITC
Auto-focus settings			
LaserAutofocus	x	x	x
Offset	1.0	1.0	1.0
Gain	40	40	40
Z-axis Relative Displacement	100 µm	100 µm	100 µm
Data points	2000	2000	2000
Sampling Rate	12000 Hz	12000 Hz	12000 Hz
Algorithm type	Double threshold	Double threshold	Double threshold
Use Rolling average	On	On	On
Rolling average size	20	20	20
Montage Capture Setup			
Active	x (4 frames)	x (4 frames)	x (4 frames)
Frames width	2	2	2
Frames height	2	2	2
Use laser autofocus during capture every 4 frames starting at frame 1	x	x	x
Dye setup			
Numerator	Exposure 0.015s	Exposure 0.01s	Exposure 0.1s
Gain	0	0	0
Offset	255	255	255
Exposure mode	Capture=on	Capture=on	Capture=on
Dynamic range	200-4095	200-4095	140-3000
Wavelength	Light path = Calcein	Light path = Hoechst	Light path = TMRM
Macro:	Calcein+Hoechst	Calcein+Hoechst	TMRM
Z-position	~5200	~5200	~5200

&Neutral density filters; % indicates the transmission from lamp A and B. Filters are denoted by their center wavelength and bandwidth (*e.g.* 470/40 = center wavelength=470 nm, bandwidth=40 nm (*i.e.* ±20 nm)). **Abbreviations:** N.a. Not appropriate; ND, neutral density.

SUPPLEMENTARY REFERENCES

1. Barraca, A., Sgarbi, G., Padula, A. & Solaini, G. Glucose plays a main role in human fibroblasts adaptation to hypoxia. *Int. J. Biochem. Cell Biol.* **45**, 1356-1365 (2013).
2. Blanchet L. *et al.* Analysis of small molecule phenotypic effects using combined mitochondrial morpho-functional fingerprinting and machine learning. *Sci. Rep.* **5**, 8035 (2015).
3. Buhlman, L. *et al.* Functional interplay between Parkin and Drp1 in mitochondrial fission and clearance. *Biochim. Biophys. Acta* **1843**, 2012-2026 (2014).
4. Burbulla, L.F. **et al.** Dissecting the role of the mitochondrial chaperone mortalin in Parkinson's disease: functional impact of disease-related variants on mitochondrial homeostasis. *Hum. Mol. Genet.* **19**, 4437-4452 (2010).
5. Coussee, E. *et al.* G37R SOD1 mutant alters mitochondrial complex I activity, Ca²⁺ uptake and ATP production. *Cell Calcium* **49**, 217-225 (2011).
6. Cunnif, B. *et al.* Mitochondrial-targeted nitroxides disrupt mitochondrial architecture and inhibit expression of peroxiredoxin 3 and FOXM1 in malignant mesothelioma cells. *J. Cell. Physiol.* **228**, 838-845 (2013).
7. De Vos K.J., Allan, V.J., Grierson, A.J. & Sheetz MP. Mitochondrial function and actin regulate dynamin-related protein 1-dependent mitochondrial fission. *Curr. Biol.* **15**, 678–683 (2005).
8. Distelmaier, F. *et al.* Mitochondrial dysfunction in primary human fibroblasts triggers an adaptive cell survival program that requires AMPK- α . *Biochim. Biophys. Acta* **1852**, 529-540 (2015).
9. Distelmaier, F. *et al.* Trolox-sensitive ROS regulate mitochondrial morphology, oxidative phosphorylation and cytosolic calcium handling in healthy cells. *Antioxid. Redox Signal.* **17**, 1657-1669 (2012).
10. Distelmaier, F. *et al.* The antioxidant Trolox restores mitochondrial membrane potential and Ca²⁺-stimulated ATP production in human complex I deficiency. *J. Mol. Med.* **87**, 515-522 (2009).
11. Distelmaier, F. *et al.* Life cell quantification of mitochondrial membrane potential at the single organelle level. *Cytometry A* **73**, 129-138 (2008).
12. Eisenberg, I. *et al.* Mitochondrial processes are impaired in hereditary inclusion body myopathy. *Hum. Mol. Genet.* **17**, 3663-3674 (2008).
13. Grau, T. *et al.* A novel heterozygous OPA3 mutation located in the mitochondrial target sequence results in altered steady-state levels and fragmented mitochondrial network. *J. Med. Genet.* **50**, 848-858 (2013).
14. Heeman, F. *et al.* Depletion of PINK1 affects mitochondrial metabolism, calcium homeostasis and energy maintenance. *J. Cell Sci.* **124**, 1115-1125 (2011).
15. Hoefs, S.J.G. *et al.* NDUFA2 complex I mutation leads to Leigh disease. *Am. J. Hum. Genet.* **82**, 1306-1315 (2008).
16. Hoffmann, M. *et al.* *C. elegans* ATAD-3 is essential for mitochondrial activity and development. *PLoS one* **10**, e7644 (2009).
17. Hom, J.R., Gewandter, J.S., Michael, L., Sheu, S.S. & Yoon, Y. Thapsigargin induces biphasic fragmentation of mitochondria through calcium-mediated mitochondrial fission and apoptosis. *J. Cell. Physiol.* **212**, 498-508 (2007).
18. Jonckheere, A.I. *et al.* Restoration of complex V deficiency due to a deletion in the human TMEM70 gene normalizes mitochondrial morphology. *Mitochondrion* **11**, 954-963 (2011).
19. Komen, J.C. *et al.* (2007) Phytanic acid impairs mitochondrial respiration through protonophoric action. *Cell. Mol. Life Sci.* **64**, 3271-3281 (2007).
20. Koopman W.J.H., Distelmaier, F., Esseling, J.J., Smeitink, J.A.M. & Willems, P.H.G.M. Computer-assisted live cell analysis of mitochondrial membrane potential, morphology and calcium handling. *Methods* **46**, 304-311 (2008a).

21. Koopman, W.J.H. *et al.* Partial complex I inhibition decreases mitochondrial motility and increases matrix protein diffusion as revealed by fluorescence correlation spectroscopy. *Biochim. Biophys. Acta* **1767**, 940-947 (2007b).
22. Koopman, W.J.H., Visch, H.J., Smeitink, J.A.M. & Willems, P.H.G.M. Simultaneous, quantitative measurement and automated analysis of mitochondrial morphology, mass, potential and motility in living human skin fibroblasts. *Cytometry A* **69A**, 1-12 (2006).
23. Koopman, W.J.H. *et al.* Mitochondrial network complexity and pathological decrease in complex I activity are tightly correlated in isolated human complex I deficiency. *Am. J. Physiol. Cell Physiol.* **289**, C881-C890 (2005b).
24. Koopman W.J.H. *et al.* Inhibition of complex I of the electron transport chain causes oxygen radical-mediated mitochondrial outgrowth. *Am. J. Physiol. Cell Physiol.* **288**, C1440-C1450 (2005a).
25. Lugus, J.J., Ngoh, G.A., Bachschmid, M.M. & Walsh, K. Mitofusins are required for angiogenic function and modulate different signaling pathways in cultured endothelial cells. *J. Mol. Cell. Cardiol.* **51**, 885-893 (2011).
26. Matthews, G.D., Gur, N., Koopman, W.J.H., Pines, O. & Vardimon, L. A weak mitochondrial targeting sequence determines tissue-specific subcellular localization of glutamine synthetase in liver and brain cell. *J. Cell Sci.* **123**, 351-359 (2010).
27. Mortiboys, H. *et al.* Mitochondrial function and morphology are impaired in parkin mutant fibroblasts. *Ann. Neurol.* **64**, 555-565 (2008).
28. Nikolaisen, J. *et al.* Automated quantification and integrative analysis of 2D and 3D mitochondrial shape and network properties. *PLoS One* **9**, e101365 (2014).
29. Szklarczyk, R. *et al.* A mutation in the FAM36A gene, the human ortholog of COX20, impairs cytochrome c oxidase assembly and is associated with ataxia and muscle hypotonia. *Hum. Mol. Genet.* **22**, 656-667 (2013).
30. Tronstad, K.J. *et al.* Regulation and quantification of cellular mitochondrial morphology and content. *Curr. Pharm. Des.* **20**, 5643-5652 (2014).
31. Valsecchi, F. *et al.* Primary fibroblasts of *NDUFS4*^{-/-} mice display increased ROS levels and aberrant mitochondrial morphology. *Mitochondrion* **13**, 436-443 (2013).
32. Vogel, R.O. *et al.* Cytosolic signaling protein Ecsit also localizes to mitochondria where it interacts with chaperone NDUFAF1 and functions in complex I assembly. *Genes Dev.* **21**, 615-624 (2007).
33. Wang, X. *et al.* DLP1-dependent mitochondrial fragmentation mediates 1-methyl-4-phenylpyridinium toxicity in neurons: implications for Parkinson's disease. *Aging Cell* **10**, 807-823 (2011).
34. Wang, X. *et al.* LRRK2 regulates mitochondrial dynamics and function through direct interaction with DLP1. *Hum. Mol. Genet.* **21**, 1931-1944 (2012a).
35. Wang, X. *et al.* Parkinson's disease-associated DJ-1 mutations impair mitochondrial dynamics and cause mitochondrial dysfunction. *J. Neurochem.* **121**, 830-839 (2012b).
36. Willems, P.H.G.M. *et al.* BOLA1 is an aerobic protein that prevents mitochondrial morphology changes induced by glutathione depletion. *Antioxid. Redox Signal.* **18**, 129-138 (2013).
37. Willems, P.H.G.M., Smeitink, J.A.M. & Koopman, W.J.H. Mitochondrial dynamics in human NADH:oxidoreductase deficiency. *Int. J. Biochem. Cell Biol.* **41**, 1773-1783 (2009).
38. Yu, T., Sheu, S.S., Robotham, J.L. & Yoon, Y. Mitochondrial fission mediates high glucose-induced cell death through elevated production of reactive oxygen species. *Cardiovasc. Res.* **79**, 341-351 (2008).
39. Yu, T., Robotham, J.L. & Yoon, Y. Increased production of reactive oxygen species in hyperglycemic conditions requires dynamic change of mitochondrial morphology. *Proc. Natl. Acad. Sci. USA* **103**, 2653-2658 (2006).